NASA CONTRACTOR REPORT

NASA CR-1793

TWO-DIMENSIONAL, SUPERSONIC MIXING OF HYDROGEN AND AIR NEAR A WALL

by Charlie L. Yates

Prepared by
THE JOHNS HOPKINS UNIVERSITY, APPLIED PHYSICS LABORATORY
Silver Spring, Md. 20910
for

NATIONAL AERONAUTICS AND SPACE ADMINISTRATION • WASHINGTON, D. C. • MARCH 1971

1. Report No.
NASA CR-1793

2. Government Accession No.

3. Recipient's Catalog No.

4. Title and Subtitle
TWO-DIMENSIONAL, SUPERSONIC MIXING OF HYDROGEN AND AIR NEAR A WALL

5. Report Date
March 1971

6. Performing Organization Code

7. Author(s)
Charlie L. Yates

8. Performing Organization Report No.

9. Performing Organization Name and Address
The Johns Hopkins University, Applied Physics Laboratory
8621 Georgia Avenue
Silver Spring, Maryland 20910

10. Work Unit No.

11. Contract or Grant No.
NASR-76

12. Sponsoring Agency Name and Address
National Aeronautics and Space Administration
Washington, D.C. 20546

13. Type of Report and Period Covered
Contractor Report

14. Sponsoring Agency Code

15. Supplementary Notes

16. Abstract

Parallel injection of hydrogen at Mach 1.19 from a rectangular wall-slot into a Mach 2.1 airstream was experimentally investigated using in-stream probes. The development of pressure, temperature, composition and velocity profiles was measured to a downstream distance of 30 slot heights for two values of the hydrogen-to-air mass flux ratio: 0.088 and 0.120. From the data, there are determined the growth rates of the turbulent species, energy and momentum transfer layer thicknesses, and the decay rates of the composition, temperature and velocity maxima. The attainment of self-similarity in the case of species transfer is also examined.

17. Key Words (Suggested by Author(s))
Turbulent jet mixing
Compressible shear layer
Compressible wall jet
Supersonic mixing

18. Distribution Statement
Unclassified - Unlimited

19. Security Classif. (of this report)
Unclassified

20. Security Classif. (of this page)
Unclassified

21. No. of Pages
45

22. Price*
$ 3.00

*For sale by the National Technical Information Service, Springfield, Virginia 22151

TWO-DIMENSIONAL, SUPERSONIC MIXING OF HYDROGEN AND AIR NEAR A WALL

Charlie L. Yates

Applied Physics Laboratory, The Johns Hopkins University
Silver Spring, Maryland

SUMMARY

A fuel injection scheme for air-breathing engines employing supersonic combustion that is particularly attractive at hypersonic flight speeds is to inject the fuel from the wall parallel to the airstream. In the past, data have not been available to permit a comprehensive design of such a system on either an analytical or an empirical basis. The purpose of this experimental program was to obtain detailed information on turbulent mixing near a solid wall in a high-speed flow with a view toward establishing a basis for an analytical solution of this flow problem.

In the tests, hydrogen was injected from a rectangular wall-slot at Mach 1.19 parallel to a Mach 2.1, two-dimensional airstream such that the initial pressure of both streams was atmospheric. The stagnation temperature of the air was ambient, while the hydrogen stagnation temperature was either ambient or 960°R, resulting in two values of the hydrogen-to-air mass flux ratio: 0.120 and 0.088. Pitot-pressure, cone-static-pressure, stagnation temperature and gas sampling probe data were obtained across the flow for downstream distances up to 30 slot heights. From these data, pressure, temperature, composition and velocity profiles were deduced and used to determine certain characteristics of the turbulent mixing process.

The data show that a decrease in the hydrogen-to-air mass flux ratio at a constant value of the momentum flux ratio results in increased mixing, which is exemplified by both the higher growth rates of the mixing layer thicknesses and by the larger decay rates of the maxima of velocity and species composition. Beyond the transition region, the mixing layers were found to grow nearly linearly, with the species and energy layer thicknesses being nearly identical and greater than the momentum layer thickness. In addition, the species composition profiles appeared to approach a condition of similarity within the distance covered by the tests.

INTRODUCTION

Among the possibilities for gaseous fuel injection into the supersonic combustors of scramjet engines is that of injecting the fuel downstream and adjacent to the combustor wall (Fig. 1). The main advantage of this approach, compared with injection from a wall at an angle to the air stream or instream injection devices, is the smaller momentum loss incurred with this scheme since strong shock waves can be largely avoided. This consideration is particularly important at high flight speeds where the momentum added via combustion is a relatively small portion of the total available. On the other hand, the slower mixing rate expected for this geometry raises important questions on the combustor length required for complete chemical reaction and the flow field quality at the inlet to the exhaust nozzle. From a more general viewpoint, this geometry, which is conventionally called the two-dimensional, turbulent wall jet, is of practical interest because of its possible application to boundary layer control and to film cooling.

Several studies (e.g., Refs. 1 to 4) have been made of the wall jet under the condition of subsonic injection and freestream velocities. These have usually shown that the flow field could be divided into two distinct regions: 1) the wall-adjacent or inner flow region, in which the wall influence is operative; and 2) the outer flow region, which behaves similar to the planar free mixing layer. Moreover, it has been shown that scale factors can be defined for each region of the flow such that they exhibit self-similarity characteristics similar to those found for the pure flows (i.e.,the flat-plate boundary layer and the planar, free mixing layer).

Studies have been made of subsonic injection into a supersonic primary flow, with particular emphasis on film cooling (Ref. 5) and boundary-layer control (Ref. 6). Relatively few studies have been made for the case of supersonic primary and secondary flows (Refs. 7 and 8). In general, the studies conducted for the supersonic case have not been of great detail in terms of measuring the complete flow field character. As a result, sufficient information was not available to guide analytical solutions of this flow problem. The present work was undertaken to provide the more detailed flow field data that are required for a successful analytical treatment.

The present results were obtained for hydrogen injection at Mach 1.19 into a Mach 2.1 airstream. In-stream probe measurements are used to deduce the development of pressure, temperature, concentration and velocity profiles for two conditions of injectant-to-airstream mass flux ratio (0.088 and 0.120). From these profiles, there are determined integral flow properties, the widths of the turbulent transfer layers and the decay rates of maximum velocity, temperature and hydrogen mass fraction.

The author is grateful for the contributions of Dr. Joseph A. Schetz, Consultant, who proposed the research program and offered many helpful suggestions during its performance. The valuable assistance of Mr. James M. Cameron in the experimental work is also gratefully acknowledged.

NOMENCLATURE

a	slot height, ft
C_p	cone-static probe pressure coefficient
F	shear force per unit area, lb_f/ft^2
h	static enthalpy, Btu/lb
H	stagnation enthalpy $\equiv h + u^2/2$, Btu/lb
j	turbulent mass flux in normal direction, $lb_m/sec\text{-}ft^2$
M	Mach number
$\mathfrak{M}$	molecular weight
p	static pressure, lb_f/ft^2
p_t'	pitot-pressure, lb_f/ft^2
q	turbulent heat flux in normal direction, $Btu/sec\text{-}ft^2$
r	temperature probe recovery factor
R	Reynolds number $\equiv \rho u a/\mu$
$\mathfrak{R}$	gas constant
T	temperature, °R
T_t'	measured stagnation temperature, °R
$\bar{T}_t$	$\bar{T}_t \equiv (T_{t_e} + T_{t_j})/2$
u	axial velocity, ft/sec
v	normal velocity, ft/sec
$\bar{x}$	axial distance from slot exit plane, ft
x	dimensionless axial distance $\equiv \bar{x}/a$
X	species mole fraction
$\bar{y}$	vertical distance from test section upper wall, ft
y	dimensionless vertical distance $\equiv \bar{y}/a$
y_e	dimensionless location of transfer layer
$\tilde{y}$	$\tilde{y} \equiv y/(y_e)_{H_2}$

$\bar{z}$	distance from centerline toward sidewall
α	$\alpha \equiv \rho u H$, Btu/sec-ft^2
β	mass flux ratio $\equiv \rho_j u_j / \rho_e u_e$
γ	specific heat ratio
Δ^*	$\Delta^* \equiv \int_0^y [1 - (\rho u/\rho_e u_e)] dy$
δ^*	dimensionless displacement thickness $\equiv \int_0^{y_e} [1 - (\rho u/\rho_e u_e)] dy$
δ_H	dimensionless energy thickness $\equiv \int_0^{y_e} [(H/H_e) - 1] (\rho u/\rho_e u_e) dy$
Θ	$\Theta \equiv \int_0^y \varphi \, dy$
Θ^*	$\Theta^* \equiv \int_0^{y_e} \varphi \, dy$
θ	dimensionless momentum thickness $\equiv \int_0^{y_e} [1 - (u/u_e)] (\rho u/\rho_e u_e) dy$
μ	viscosity, lb$_m$/ft-sec
ρ	density, lb$_m$/ft^3
τ	shear stress, lb$_f$/ft^2
φ	$\varphi \equiv (p/\rho_e u_e^2) + [(u/u_e) - 1] (\rho u/\rho_e u_e)$
ω	species mass fraction
$\tilde{\omega}$	$\tilde{\omega} \equiv 1 - [\omega_{H_2} / (\omega_{H_2})_w]$

<u>Subscripts</u>

c	cone probe condition
e	freestream condition
H_2	hydrogen condition
i	i-th species
j	injectant (H_2) condition
s	shock condition
t	stagnation condition
w	wall condition

EXPERIMENTAL APPARATUS AND PROCEDURE

Test Model and Facility

A schematic of the two-dimensional experimental model, including important dimensions, is shown in Fig. 2. The installed model is shown in Fig. 3 with the near-side window frame removed. The model was fabricated of uncooled, stainless steel except for the two nozzle blocks, which were constructed of nickel and had water-cooling passages in their throat regions. It was intended that the model be capable of withstanding the heating loads associated with short-duration combustion tests; hence, a heat-sink approach was used and all components were heavy-walled. Each side-wall was equipped with two 3-inch-diameter, heat-resistant windows of Schlieren quality mounted eccentrically in removable frames which could be rotated 180°, so that the complete length of the test section could be observed in successive tests. The contoured block of the air half-nozzle was graphically designed by the method of characteristics (Ref. 9), assuming uniform flow at the throat section and neglecting boundary layer effects. The design Mach number was 2.10.

The removable injector box was equipped with a 0.265-inch-thick aerogrid plate containing 196 holes on equal-area centers. Each hole consisted of a 0.055-inch-diameter x 0.077-inch-long cylindrical inlet followed by a diverging section whose included angle was 20°. The aerogrid, which was operated in a choked-flow condition, provided a nearly uniform flow across the injector nozzle exit plane. Two stiffening rods, which can be seen in Fig. 3, were provided between the splitter plate and the upper block of the injector nozzle 0.193 inch upstream of the exit plane. The injector design Mach number (M_j) of 1.19 was chosen for the following reasons:

1) To minimize disturbances at the injector lip, the pressure in the two streams were matched by presetting plenum conditions in each. To avoid pressure communication back to the respective plenums, both streams had to be sonic or supersonic, i.e., $M_j \geq 1.0$.

2) In the case of combustion tests, M_j should be kept relatively low, so that the injectant static temperature would not be greatly reduced (thereby degrading ignition conditions).

The upper wall of the test section was provided with 13 static pressure taps, whose spacing varied from $\sim$ 0.6 inch near the injector exit plane to 1.0 inch at a downstream distance of 8.0 inch and beyond. Five static pressure taps were spaced along the contoured air nozzle block. Ten thermocouple assemblies were spaced at intervals of 1.0 inch or less along the test section upper surface, 3 were located in the nozzle section, and 3 were brazed to the air side of the splitter plate in the plane of the stiffening rods. The sheaths of the latter 3 can be seen passing thru the injector flow area in Fig. 3. Thermocouples and pressure taps were also located in the air plenum and below the aerogrid in the injector plenum.

The experiments were conducted at the APL Propulsion Research Laboratory. Compressed air, which was filtered and dried, was stored in torpedo flasks at 2000 psi. The air was supplied to the test area through remotely operated valves. The hydrogen was supplied through remotely controlled valves from a tank trailer. Hydrogen heating was provided by a nickel tube that was resistance-heated. The 384-inch-long, 0.500-inch I.D. x 0.312-inch-wall, thermally insulated tube acted as a resistance element in a D.C. circuit. This heater was operated in a blowdown mode. The exhaust from the model was discharged through a steam ejector exhaust system.

Flow Field Instrumentation

The in-stream instrumentation (Figs. 3 and 4) consisted of seven-point pitot-pressure, stagnation-temperature and gas-sampling rakes, whose probe tips were spaced at 0.203 inch center-to-center, and a five-point cone-static-pressure rake with a probe spacing of 0.281 inch (the eight-point pitot-pressure rake shown in Fig. 4 was used in the initial part of the program). All probes were constructed of stainless steel. The pitot-pressure probes were fabricated of 0.065-inch O.D. x 0.009-inch-wall straight tubing. The same size tubing was used for the gas sampling probes; however, the probe tips were spun at a 15° half-angle to give a 0.015-inch inlet diameter, which resulted in an internal expansion area ratio of 9.8:1. The stagnation temperature probes consisted of chromel-alumel thermocouples in a 0.102-inch O.D. x 0.020-inch-wall tube. The tube tips were spun at a 15° half-angle to an inlet diameter of 0.030 inch. Four 0.008-inch-diameter, equally-spaced bleed holes were drilled around the probe circumference in a plane 0.062 inch aft of the thermocouple junction. The 0.125-inch-O.D., cone-static-pressure probes had 15° half-angle tips. Four 0.015-inch-diameter, equally-spaced pressure ports were located 0.170 inch from the tip and fed to individual pressure instruments. The probe rakes were operated in pairs, with the two pressure rakes being used together. The two rakes were mounted 0.72 inch to each side of the test section centerline ($\bar{z} = +0.72, -0.72$) such that their tips were in the same $\bar{y}$, $\bar{z}$ plane. They could be moved manually, 0.34 inch in the vertical ($\bar{y}$)direction and 8.0 inches in the axial ($\bar{x}$) direction. In the initial tests, the probe blockage was sufficiently large to produce a standoff shock. To avoid this problem, transverse holes were drilled in the rake bodies (Fig. 4) to bleed the high pressure field between the probes to the lower pressure outboard region. With the holes present, no standoff shock was observed.

The pressure transducers and thermocouple output signals were stored on magnetic tape by a digital data acquisition system which records at the rate of 50 channels per second, and some channels were simultaneously recorded on strip-chart recorders. The gas samples were collected in evacuated bottles which were valved for remote operation. Subsequent to a test, the samples were analyzed on a gas chromatograph. Several improvements in the gas chromatography equipment and techniques were made during this program (Ref. 10).

Test Procedure

The tests were conducted from a remote control area. The air flow was initially set such that the air nozzle static pressure was atmospheric in the plane of the injector exit. The facility exhauster was then started, after which the hydrogen flow was established at a level required to give atmospheric static pressure at the injector exit. Data were taken for a period of 10 seconds, which was the minimum time required to obtain sufficiently large gas samples. In tests where heated hydrogen was used, the heater was preheated to 1100°R, which was sufficient to heat the supply lines and still permit a maximum temperature of 1050°R to be attained in the injector plenum. Data were taken during the time that the injector plenum temperature decreased from 1010 to 910°R, a period of 10 seconds. After a test, the probe type and/or position was changed, and the procedure was repeated.

EXPERIMENTAL RESULTS

Measured Data

Test Conditions - Table I shows the test conditions employed and the legend used to plot the data in subsequent figures. The air and hydrogen Mach numbers were 2.10 and 1.19, respectively, throughout the program. Air plenum conditions were held essentially constant at T_{t_e} = ambient and $p_{t_e} = 135$ psia. Variations in T_{t_e} of 72°R reflect daily and seasonal temperature changes (the data were collected over a one year period), while the ± 2 psi fluctuation in p_{t_e} was the degree of test repeatability. The hydrogen plenum pressure, p_{t_j}, was nominally 35.5 psia; however, fluctuations of as much as ± 1.5 psi were accepted in order to decrease the time required for more exact flow rate settings and thereby conserve the hydrogen supply. The only planned change in test conditions was applied to the hydrogen plenum temperature, T_{t_j}, for which two values were tested: ambient ($560° \pm 25°$R) and 960°R. Again, daily and seasonal variations are seen in the ambient temperature, which was usually 20 to 30°R higher than T_{t_e} due to different storage environments. For the hot hydrogen case, T_{t_j} is a time-averaged test condition (see *Test Procedure*).

The experiments were conducted in three series as follows: Series 1: T_{t_j} = ambient, $x = 2$ to 7; Series 2: T_{t_j} = ambient, $x = 10$ to 30; and Series 3, $T_{t_j} = 960°$R, $x = 10$ to 30. (Here $x \equiv \bar{x}/a$, where $\bar{x}$ is axial distance from the slot exit plane, and a is slot height, 7/32 inch.) Data were taken for values of $y = 0$ to 6 ($y \equiv \bar{y}/a$, where $\bar{y}$ is vertical distance from the upper wall). The order of run numbers in Table I is explained by the fact that Series 2 was actually conducted prior to Series 1. In order to identify the data in subsequent figures, the information contained in Table I has been used to define average test conditions for each of the above series, and these conditions are listed in Table II together with some ideal, initial flow properties that will be useful in future discussions. The parameter chosen to identify the data is $\beta \equiv \rho_j u_j / \rho_e u_e$, which is ~ 0.120 for ambient temperature and 0.088 for $T_{t_j} = 960°$R.

Schlieren Pictures - A limited number of Schlieren photographs was taken for the purpose of studying qualitative features of the flow field. Figure 5 shows a typical photograph, which was taken for $\beta = 0.120$ (the probe tips are located at $x = 10$). The portion of the mixing region in which large gradients in the flow occur is clearly discernible. The finite thickness of the splitter plate causes a disturbance in the flow field, even though the pressures are equal at the point of injection. One also sees evidence of disturbances within the air nozzle that apparently influenced the downstream flow development. These disturbances are caused by a normal gradient in Mach number at the nozzle throat inlet brought about by the small radius of curvature in that region (refer to Fig. 2). (A uniform flow in the throat region was assumed in the nozzle design calculations.)

Pitot- and Cone-Static-Pressure Data - Figure 6 shows pitot-pressure data for each of three β's. For each x, data were taken for 3 vertical locations of the pressure rake. The pressure scales for various x's are displaced for the sake of clarity. Significant time-wise pressure fluctuations were observed in the high gradient region of the flow, and they are indicated in Fig. 6 by the data brackets which show the maximum extent of the fluctuations and the time-averaged pressure. The pressure data signals were sampled once every 2.25 sec, and either 4 or 5 data points per test condition were made. The average value was obtained by assuming a linear, time-wise variation between points.

The relatively long time between points and their small number make it possible that neither the extents of fluctuation nor the time-averaged values of pitot pressure were precisely determined, particularly for $\beta = 0.088$ (Fig. 6c), where both the fluctuations and the region of unsteady pressure are relatively large. Therefore, personal judgement was used in defining time-averaged pressure profiles over the unsteady region by drawing smooth curves within the limits of fluctuations but not necessarily through the individual time-averaged data points. The nonuniformity in these profiles outside the mixing region gives evidence of flow field disturbances; moreover, pressure fluctuations are observed at some points of the unmixed flow. Apparently in some cases these disturbances occurred near the outer edge of the mixing region, which further complicated the task of defining time-averaged profiles and led to some uncertainty in the definition of the edges of the transport layers. The cone-static-pressure data in Fig. 7, unlike the pitot-pressure data of Fig. 6, do not show the existence of unsteadiness in the flow.

Gas Sample Data - The gas sample data shown in Fig. 8 include only those points that indicated at least a trace of hydrogen. Some of the scatter in these data is attributed to small leaks in the sample collection system which could have occurred during the time between sample collection and sample analysis. It is believed that the preferential effusion of hydrogen due to its low molecular weight resulted in erroneously low hydrogen concentrations. Accordingly, the curves in Fig. 8 were drawn through the points which show the highest percentage of hydrogen. Even so, it was necessary to repeat many tests before the curves could be reasonably defined, especially with the heated hydrogen ($\beta = 0.088$), and some data points were discarded (not shown).

Stagnation Temperature Data - Useful stagnation temperature data were obtained only for the case of $\beta = 0.088$, where T_{t_j} was controlled, and the results are shown in Fig. 9. Two data points shown for $x = 30$, $y < 1$ were not used to define the curve for $x = 30$ since they were inconsistent with other points taken in the same region and their use in subsequent calculations resulted in unrealistic flow property profiles. It is believed that a faulty thermocouple junction caused the low readings (the three uppermost data points at $x = 30$ were all measured with the same thermocouple). In the other cases with unheated hydrogen (and air), the run-to-run variations in stagnation temperatures were of the same magnitude as the temperature variations across the flow field.

Hence, it was not possible to define meaningful profiles. In these cases, the stagnation temperature was assumed constant throughout the flow for the purpose of data analysis. This constant temperature was taken as an arithmetic average of T_{t_j} and T_{t_e}, and is listed in Table II as $\bar{T}_t$. An arithmetic average temperature was favored over, say, a mass-averaged value since the former led to more accurate calculations of H_2 mass flux for the relatively small downstream distances ($x \leqq 30$) over which data were taken. (The significance of an accurate H_2 mass determination is discussed in Reliability of Results.) The mass-averaged temperature, which would essentially equal T_{t_e}, would obviously be more appropriate for large downstream distances.

Hydrogen Slot Calibration - In some tests, the hydrogen flow rate was measured with a calibrated metering venturi. From these tests, it was possible to calculate the effective throat area of the hydrogen slot, the result being a discharge coefficient of 0.90. This value was used to calculate hydrogen flow rate in all other tests using the measured plenum conditions and the known sonic flow relationships.

Deduced Flow Field Properties

The static pressure, static temperature, and velocity profiles shown in Figs. 10-12 were calculated from the curves drawn in Figs. 6-9, respectively, based on increments of $y = 0.25$ or less, as described in the Appendix. Because the shocks from adjacent cone probes would fall on or ahead of the cone surface pressure taps at $M \leq 1.36$, the static pressures had to be estimated for $M \leq 1.36$. The estimated values, indicated by crosshatching in Fig. 10, were based on the following criteria: 1) the value and gradient of the deduced pressure at the upper limit of y ($M = 1.36$) controlled the extension of the profile into the region of smaller y, unless this procedure was negated by other considerations; 2) at $y = 0$, the pressure was set equal to the measured wall value, with $\partial p/\partial y = 0$ near the wall, in accord with boundary layer theory; and 3) for intermediate values of y, the estimation was somewhat arbitrary except for the restrictions of an upper limit on pressure imposed by the measured pitot pressure, and a lower limit imposed by the lowest possible ratio of static-to-pitot pressure that corresponded to $M \leq 1.36$. (The validity of this procedure is discussed in Reliability of Results.)

The deduced static temperature profiles for the heated hydrogen case ($\beta = 0.088$) in Fig. 11 show the cooling effect of the massive wall, especially at $x = 30$. It is interesting that the velocity profile at $x = 2$ in Fig. 12a shows the wake-like character of the flow generated by the finite thickness of the splitter plate. It is also noted that the flow property profiles do not become equal to their freestream values in a regular manner, a fact that will eventually be related to flow-field disturbances.

DISCUSSION OF RESULTS

Reliability of Results

A sensitive test of the general validity of the experimental measurements and the foregoing deduced flow property profiles in those regions where hydrogen is present is established by integrating the H_2 mass flux distributions of Fig. 13 and comparing the results with the independently measured H_2 flow rates. The integrations from Fig. 13 were done with a planimeter, and the results are shown on the figure. For $x \geq 7$, the deduced H_2 flow rates agree with the measured values to within $\pm$ 10%, which is considered quite good. The differences at $x < 7$ were $\leq$ 19%. In general, the differences can be related to the following effects, some of which are particularly important at small x:

1) the necessity to estimate static pressure over a relatively large portion of the region in which hydrogen is present (this effect does not account for the high flows deduced for $x = 2$ and 7, since in those cases the lowest possible pressure consistent with the pressure data was assumed over most of the subject region);

2) the lack of detailed knowledge of the temperature field for cases where unheated hydrogen was used, which introduced some error in the results, especially at small x, where there occurred the largest differences between the actual stagnation temperature and the average value used in the calculations;

3) the relatively large errors in local mass flux due to small errors in the measured hydrogen mole fraction that could possibly occur in regions where the mole fraction was high ($\sim$ 0.9); and

4) departure of the velocity field from one-directionality.

At small x, the third of the above effects was probably the most significant. For example, for $x = 2$ and $y = 1$, the following conditions lead to a mass flux of 20.5 lb/sec-ft^2: $p = 16.5$ psia, $p_t' = 32.6$ psia, $T_t = 543^\circ R$ and $X_{H_2} = 0.947$. If the latter conditions, excluding p_t', are successively varied, the following results are obtained: 1) a 30% decrease in p to 11.5 psia, which gives a permissible M of 1.337, gives a 4.9% decrease in hydrogen mass flux; 2) a 2.8% increase in T_t to $558^\circ R$, which was the average hydrogen plenum temperature, gives a 1.3% decrease in mass flux; and 3) a 1.1% decrease in X_{H_2} to 0.937 gives a 4.7% decrease in mass flux.

Significance of Results

Some interesting aspects of the experimental results lie in the behavior of certain gross features of the flow field such as its integral properties, the absolute and relative growth rates of the transfer layers for species, heat and momentum, the decay rates of maximum velocity, temperature and hydrogen mass fraction, and the dependence of these various properties on initial flow conditions. In order to determine the edges of the transfer layers, it is important that the proper flow properties be examined. For example, the edge of the turbulence-produced momentum transfer layer is not sufficiently determined by the edge of the velocity layer, since the velocity field can also be affected by pressure gradients and compressibility. The correct approach must be based on an application of the mean flow conservation equations. For this purpose, it is assumed that use of the boundary-layer approximation to the steady-state conservation equations (Ref. 11) is valid, with the exception that the normal pressure is not neglected. The particular forms of the mean flow equations that are used in this discussion are as follows:

Mass

$$\partial(\rho u)/\partial x + \partial(\rho v)/\partial y = 0 \tag{1}$$

Species

$$\partial(\rho u\ \omega_i)/\partial x + \partial(\rho v\ \omega_i)/\partial y = - \partial j_i/d_y \qquad i = H_2\text{, air} \tag{2}$$

Energy

$$\partial(\rho uH)/\partial x + \partial(\rho vH)/\partial y = - \partial q/\partial y \tag{3}$$

Momentum

$$\partial(\rho u^2)/\partial x + \partial(\rho vu)/\partial y = - \partial p/\partial x - \partial\tau/\partial y \tag{4}$$

The simplified form of the energy equation is for flows with laminar and turbulent Prandtl and Lewis numbers equal to one. Although these conditions do not in general exist for the present results, the simplicity introduced by these restrictions is considered to be warranted in view of the overall accuracy of measurements and the presumably small effect on the overall conclusions. The species mass flux j_i, heat flux q and shear stress τ, all of which in general include both molecular and turbulent contributions, are assumed to be dominated by turbulent transport. In general, the edges of the species, energy and momentum transfer layers are, respectively, defined as the minimum values of y at and beyond which j_i, q and τ and their y-derivatives vanish. In initial treatments of the present data, it was assumed that the normal velocity component v was negligible throughout the flow, in which case Eqs. (2) to (4) reduce to the following forms for parts of the flow at the edge and outside the transfer regions:

Species

$$\partial(\rho u\ \omega_i)/\partial x = 0 \tag{5}$$

Energy

$$\partial(\rho uH)/\partial x = 0 \tag{6}$$

Momentum

$$\partial(p + \rho u^2)/\partial x = 0 \tag{7}$$

Equations (5) to (7) all have the form, $\partial\xi/\partial x = 0$, where ξ is a particular flow property. They show that the procedure to be used in defining the transfer layer edge at a particular x is to determine the value of y at which ξ equals its initial value and beyond which $\partial\xi/\partial x = 0$. However, this procedure was found unsatisfactory, one reason being the existence of a sizable normal velocity, which can be implied qualitatively from the results as follows. Equation (1) can be integrated between $y = 0$ and $y =$ constant to give

$$\rho v/\rho_e u_e = - \partial \left[\int_0^y (\rho u/\rho_e u_e) dy\right] \Big/ \partial x$$

$$= \partial\left\{\int_0^y [1 - (\rho u/\rho_e u_e)] dy\right\} \Big/ \partial x \equiv \partial\Delta^*(x,y)/\partial x \tag{8}$$

Equation (8) expresses the normalized (by $\rho_e u_e$ = constant), normal mass flux across a particular horizontal plane in terms of the local, axial gradient of an integral property, which has been defined as $\Delta^*(x,y)$. Moreover, the equation provides a means of determining local streamline deflection. Ideally, the integrand in Eq. (8) would be essentially equal to zero for values of y greater than the thickness of the mixing region. In this case, Δ^* for a given x would approach a constant value that is conventionally defined as the (nondimensional) displacement thickness, $\delta^*(x)$. The values of Δ^* in Fig. 14 were obtained from the data by graphical integration from $y = 0$ to $y = 5.75$ using a planimeter. It will be established later that the thickness of the mixing layer never exceeded $y = 5.75$ for the region in which data were taken; hence, Δ^* would be expected to have reached an essentially constant value by $y = 5.75$. Figure 14a shows that, for $\beta = 0.120$,[a] this result was realized for $x \leq 20$, but not at $x = 30$. The result was not realized at all for the $\beta = 0.088$ case (Fig. 14b).

With regard to the actual determination of v, the profiles for Δ^* are not for sufficiently small increments of x to permit differentiation; nevertheless, some qualitative results can be obtained by considering differences between the profiles. For example, values of Δ^* in the region $y = 0$ to ~ 1 are nearly independent of x, implying that the flow is nearly parallel to the wall. Furthermore, the thickness of this parallel flow region grows as x increases. On the other hand, v has both positive and negative values outside the parallel flow region. For example, the profiles for $\beta = 0.120$ at $x = 0$ and 2 show that $\partial\Delta^*/\partial x$ (and, hence, v) is positive (downward) for $y \simeq 1$ to 2.3 but is negative for $y > 2.3$. For x between 2 and 4, v becomes positive for all values of y beyond the parallel flow region. However, for x between 4 and 7, there again appear both positive ($y \simeq 1.5$ to 3) and negative ($y > 3$) v. For $x > 10$, v is apparently positive for all y outside the parallel region. This last statement appears to hold as well for $\beta = 0.088$. Furthermore, the results obtained for $\beta = 0.088$ suggest that as β is decreased, the thickness of the parallel-flow region near the wall is increased, but the magnitude of v is increased in a large portion of the flow field outside this region (i.e., for $y \gtrsim 2.3$).

Because Δ^* at a given x does not always approach a constant value within the data region, it is impossible to determine displacement thickness at all x's. What has been done is to determine δ^* at $y = 5.75$, and these values are shown for each β in Fig. 15a, which more clearly shows how the sign and magnitude of v on the $y = 5.75$ plane varies with x and β. The values of $\delta^*(x = 0)$ are computed from the ideal, initial flow conditions, and they are simply: $\delta^*(x = 0) \approx 1 - \beta$. The slope of the curve shown in Fig. 15a for $\beta = 0.120$ implies that v is negative for $0 < x \lesssim 2$ and $4 \lesssim x \lesssim 7$ and positive for $2 \lesssim x \lesssim 4$ and $x \gtrsim 7$. Since the Mach angle is 28.4° for the Mach 2.10 external air flow, any disturbance generated at the injection station should not affect the flow at $y = 5.75$ until $x \geq 8.8$. Hence, the fact that changes in v occur upstream of $x = 8.8$ indicates the presence in the flow of preexisting disturbances, as were seen in the Schlieren photograph of Fig. 5. (Further evidence of such disturbances is discussed later.) Approximate values of v between $x = 20$ and 30 can be calculated by assuming a linear variation of δ^* between these two stations. When this is done, one finds $\rho v/\rho_e u_e = 0.049$ and 0.066 for $\beta = 0.120$ and 0.088, respectively. Using the values of ρ computed from the data at $x = 20$, the above values correspond to $v = 85$ ft/sec and 90 ft/sec, respectively.

---

[a] Hereafter, "$\beta = 0.120$" indicates both Series 1 and Series 2 tests.

Returning to the transfer equations, we find that Eqs. (2-4) can be integrated over y and then combined with Eq. (8) to give:

Species

$$j_i = \omega_i \, \partial\left(\int_0^y \rho u dy\right)\Big/\partial x - \partial\left(\int_0^y \rho u \omega_i dy\right)\Big/\partial x \qquad (9)$$

Energy

$$q - q_w = H \, \partial\left(\int_0^y \rho u dy\right)\Big/\partial x - \partial\left(\int_0^y \rho u H dy\right)\Big/\partial x \qquad (10)$$

Momentum

$$\tau - \tau_w = u \, \partial\left(\int_0^y \rho u dy\right)\Big/\partial x - \partial\left[\int_0^y (p + \rho u^2) dy\right]\Big/\partial x \qquad (11)$$

where the subscript w refers to wall conditions. When the requirements $j_i = q = \tau = 0$ are put on Eqs. (9) to (11), we obtain the conditions that must exist at and beyond the transfer layer edges. For example, the edge of the species transport layer is given by the value of y that satisfies the condition:

$$\omega_i \, \partial\left(\int_0^{y_e} \rho u dy\right)\Big/\partial x = \partial\left(\int_0^{y_e} \rho u \omega_i dy\right)\Big/\partial x \qquad (12)$$

The important thing to note about Eq. (12) is that $\omega_i = 0$ is not a necessary condition for vanishing species transport. Rather, Eq. (12) requires only that changes in the axial convective flux of the species be balanced by an equal change in the normal convective flux. Obviously, Eq. (12) and the corresponding forms of Eqs. (10) and (11) can not be used with the present data, since the data are insufficient for meaningful differentiation. However, to account at least partially for the normal convective flux, the assumption is made that the following conditions are approximately satisfied near the transport layer edges:

$$\omega_i \approx \omega_{i_e} ; \quad H \approx H_e ; \quad u \approx u_e \qquad (13)$$

When these conditions are applied to the normal convective terms in Eqs. (9) to (11), the following criteria for determining the transfer layer edges result:

Species

$$\partial\left(\int_0^{y_e} \rho u \omega_i dy\right)\Big/\partial x = 0, \ i = H_2 \qquad (14)$$

Energy

$$\partial\left(\int_0^{y_e} [(H/H_e) - 1](\rho u/\rho_e u_e) \, dy\right)\Big/\partial x \equiv \partial\delta_H(x)/\partial x = q_w/\rho_e u_e H_e \qquad (15)$$

Momentum

$$\partial\left(\int_0^{y_e} \{[p/\rho_e u_e^2] + [(u/u_e) - 1][\rho u/\rho_e u_e]\} \, dy\right)\Big/\partial x \equiv \partial\Theta^*(x)/\partial x = \tau_w/\rho_e u_e^2 \qquad (16)$$

Equations (14-16) define the transfer layer edges, y_e, as the values of y at which the axial gradient of an integral property equals a local, wall boundary condition. Since these boundary conditions are independent of y, the values of these integrals should remain constant when their upper limits are extended beyond y_e.

Species Transfer Layer - The edge of the hydrogen transport layer is simply the locus of points at which the mole fraction goes to zero, in Fig. 8, and these values of y_e are shown in Fig. 16 for the two values of β. For $\beta = 0.120$, the species layer grows at a decreasing rate for x between 0 and ~ 10, after which it grows at a nearly constant rate, $dy_e/dx \simeq 0.075$. For $\beta = 0.088$, y_e is larger and the nearly constant growth rate is $dy_e/dx \simeq 0.085$.

Energy Transfer Layer - Distributions of the integrand of Eq. (15) are plotted in Fig. 17a for $\beta = 0.088$, which is the only case for which detail temperature data are available. It is seen that, for each value of x, the value of the integrand becomes essentially equal to zero at a rather well-defined value of y. To demonstrate the importance of using the proper parameter to define the transport layer edge, distributions of $\alpha (\alpha \equiv \rho u H)$ are plotted in Fig. 17b. It was shown earlier that if the normal velocity v were negligible, α would be the proper quantity to use for identifying the energy layer edge. However, Fig. 17b shows that α does not approach a constant value at a well-defined y. One might interpret the distributions of α to mean that the energy layer edge occurs at the point (greater than $y = 1$) where α reaches its maximum value immediately following the region in which α rapidly increases. When this is done, however, the deduced layer thickness is significantly smaller than that determined from the distributions of $[(H/H_e) - 1] (\rho u/\rho_e u_e)$. The energy layer thickness determined from Fig. 17a has been plotted in Fig. 16, where it is seen that this layer is almost identical to the species transfer layer. (When α is used to define the energy layer, its thickness is more nearly equal to that of the momentum transfer layer, which is discussed in the next paragraph.) Values of the integral δ_H defined in Eq. (15) were also computed from the data for $\beta = 0.088$ and these are plotted in Fig. 15b. Observe that the axial gradient of δ_H, which is conventionally called the energy layer thickness, is proportional to the wall heat flux. It is interesting that the data show a nearly linear variation of δ_H, implying a constant wall heat flux of 4.6 Btu/sec/ft^2.

Momentum Transfer Layer - The integrand of Eq. (16), which we will call $\varphi(x,y)$ for brevity, is plotted in Fig. 18 for $\beta = 0.120$, $x = 2$ and 10, and for $\beta = 0.088$, $x = 10$. These distributions are typical of those computed from the data, and they show the difficulty that is encountered when an attempt is made to define the momentum transfer edge from them, i.e., the integrands do not approach a constant value at any y. The erratic behavior of φ is believed due to pressure disturbances in the flow that obviously affect φ considerably more than they affect quantities related to heat transfer, a result that is generally true for shock waves. Hence, an alternative approach is required to determine the momentum layer. For this reason, attention must be focused on Eq. (11), rather than Eq. (16).

It is first observed that, whereas φ behaves erratically, the integral of φ for varying values of the upper limit y results in relatively smooth distributions (this will be demonstrated shortly). However, Eq. (11) can not be expressed in terms of φ without further approximation. Hence, it is assumed that the normal convection term can be approximated for all y as follows:

$$u\partial\left(\int_0^y \rho u dy\right)\Big/\partial x \approx u_e \, \partial\left(\int_0^y \rho u dy\right)\Big/\partial x \tag{17}$$

We will eventually be interested in the integral of φ only in the region of the transfer layer edge, in which case the approximation of Eq. (17) is reasonable. It is also observed, with reference to Eq. (11), that it can no longer be assumed that $\tau = 0$ holds for any portion of the measured flow, since τ also includes the shock-generated shear stress, i.e., $\tau = \tau_t + \tau_s$, where τ_t is due to the turbulent mixing process and τ_s is due to shock waves. Thus, we must consider the equation

$$(\tau_w - \tau)/\rho_e u_e^2 \approx \partial\left(\int_0^y \varphi dy\right)\Big/\partial x \equiv \partial\Theta(x,y)/\partial x \tag{18}$$

Equation (18) can be integrated over x to give the following result

$$F(x,y) \equiv \int_0^x (\tau_w - \tau)\, dx = \rho_e u_e^2 [\Theta(x,y) - \Theta(0,y)] \tag{19}$$

This equation has the following physical interpretation: First, consider a fluid element bounded by vertical planes at $x = 0$ and x and by horizontal planes at $y = 0$ (the wall) and y. Then, Eq. (19) expresses the total shear force per unit area, $F(x,y)$, acting on the element as the change, between 0 and x, of an integral whose upper limit is y. At this point, it might be argued that, for a given x: 1) τ_s is independent of y, i.e., the shock disturbances have equally affected all parts of the flow in a vertical plane; and 2) $\tau_t \gg \tau_s$ for a large portion of the mixing region. While neither of these arguments is thought to be totally correct, they are believed to be complementary to the extent that a significant change in the character of the shear force distribution, F, evaluated at a constant x should occur in the region where τ_t vanishes. Hence, it seems possible to identify the turbulent, momentum transfer edge with the value of y at which F changes character. This approach is explored by plotting values of $\Theta(x,y)$ in Fig. 19, where the points shown are the actual values determined from the data. Figure 19 shows that $[\Theta(x,y) - \Theta(0,y)]$ is also not well-behaved, in that it changes sign in an intractable manner. On the other hand, the distributions of $\Theta(x,y)$ themselves are relatively well-behaved. Moreover, for each x there can be seen at least two distinct portions of the $\Theta(x,y)$ distribution, in each of which a well-defined variation exists, and the two portions of which merge smoothly through a transition region. However, in order to identify an exact point along a distribution curve, the data points on both sides of the transition region were used to define two curves that were extended to an intersection point. The value of y at this intersection has been taken as the edge of the momentum transfer layer. It is noted that for some distributions in Fig. 19 there is another point at which a significant change in character occurs (e.g., $x = 7$, $y = 2$). This presumably reflects the effect of strong, local disturbances.

The momentum layer edges determined from Fig. 19 by the procedure discussed above have been plotted in Fig. 16 for the two values of β. For $\beta = 0.120$ and for the region $x > 4$, the momentum growth rate decreases to a nearly constant value of $dy_e/dx = 0.035$ at $x \geq 10$. Since the momentum layer had an unmeasured, finite thickness at $x = 0$ due to initial boundary layers, it is not possible to state the behavior of the momentum layer for x between 0 and 4. It is noted that the nearly constant growth rate of the momentum layer is only about one-half that of the corresponding species layer, which was larger for all x. For $\beta = 0.088$ and $x \geq 10$, the momentum layer again shows a nearly constant growth, in this case $dy_e/dx = 0.072$. While this growth rate is still less than those for the species and energy layers, the relative increase in growth rate due to the decrease in β is significantly larger for momentum transfer. In addition, the data suggest the possibility for $\beta = 0.088$ that the thickness of the momentum layer might even exceed that of the species layer for small x ($x < 10$), this presumably being due to increased mixing brought about by a larger, initial boundary layer in the hydrogen flow.

The locations of the momentum layer edge shown in Fig. 19 have been transferred to the corresponding φ profiles of Fig. 18. It can be seen in Fig. 18 that the layer edge is related to a region in which there occurs a large gradient in the profile. In retrospect, one might attempt to use this result to determine the layer edge directly from the φ-profiles. However, this was found to be difficult to do for the following reasons: 1) in many cases, the high gradient region extended over large y distances which made it difficult to identify an exact point with the layer edge; and 2) in some cases (not particularly those shown in Fig. 18), the high gradient region was apparently concealed by flow field disturbances to the extent that it could not be definitely identified. In this connection, it is interesting to relate the momentum layer edges shown in Fig. 19 to the velocity profiles of Fig. 12. The impossibility of consistently determining the momentum layer edge from the velocity profiles is obvious.

The values of $\Theta(x,y)$ for $y = 5.75$ have been plotted in Fig. 15c. In the absence of flow disturbance, $\partial\Theta(x,y = 5.75)/\partial x$ would be proportional to the wall shear stress, τ_w, since $y = 5.75$ is beyond the momentum transfer edge, in which case $\tau_t = 0$. Moreover, since τ_w was always negative in these tests (no flow separation), $\partial\Theta(x,y = 5.75)/\partial x$ would also be always negative. However, Fig. 15c shows, for $\beta = 0.120$, regions in which the gradient of Θ and, hence, $(\tau_w - \tau) = (\tau_w - \tau_s)$ is positive. Thus, it is concluded in this case that the flow at $y = 5.75$ was subjected to a positive shear stress, τ_s, due to shock disturbances. The disturbances were apparently absent or weaker for $\beta = 0.088$, at least for $x > 10$. Due to the presence of these flow disturbances, the data shown in Fig. 15c can not be used to estimate wall shear, τ_w.

The contribution of the pressure term to the Θ integral can be subtracted out to give the following integral:

$$\theta(x) = \int_0^{y_e} [(u/u_e) - 1]\ (\rho u/\rho_e u_e)dy$$

The integral $\theta(x)$ (or more correctly, $-\theta(x)$) is conventionally called the (dimensionless) momentum thickness. For completeness, values of $\theta(x,y = 5.75)$ have been plotted in Fig. 15d. However, this integral has very little utility for the present tests due to the presence of a sizable normal pressure gradient.

Decay of Mass Fraction, Velocity and Temperature Maxima - The decay rates of maximum hydrogen mass fraction (wall value), maximum velocity referenced to initial jet velocity, and maximum static tmperature referenced to initial jet static temperature are shown in Fig. 20. The maximum mass fraction remains at 1.0 through the transition region, the end of which occurs at approximately $x = 8$ to 9 for $\beta = 0.120$. The data indicate that transition is slightly longer for $\beta = 0.088$; however, the decay for the latter case eventually becomes larger at $x \gtrsim 23$. The transition region for velocity is essentially non-existent, undoubtedly due to the influence of boundary layers existing in the initial flow. For $x \gtrsim 12$, the velocity decay is also greater for $\beta = 0.088$. Finally, the static temperature actually rises and remains above its initial value for all x. This result is explained by the interplay of flow deceleration (rising temperature) and wall heat transfer (decaying temperature), with the latter being the controlling effect.

Study of Possible Flow Similarity - An interesting question at this point is whether or not and to what extent the flow field approaches a condition of self-similarity in the so-called fully developed flow regime, a result that is characteristic of unbounded mixing layers. This question is particularly important for the concentration profiles, since an affirmative answer would mean that the concentration field, and, hence, the extent of H_2 combustion, could be estimated for downstream distances beyond the region of measurements. Moreover, it is only in the case of the concentration profiles that possible scale factors can be easily identified and tested. For this purpose, the following dimensionless quantities are defined:

$$\tilde{\omega} \equiv 1 - [\omega_{H_2}/(\omega_{H_2})_w] \qquad \tilde{y} = y/(y_e)_{H_2}$$

where $(\omega_{H_2})_w$ is the wall value of hydrogen mass fraction and $(y_e)_{H_2}$ is the species layer edge. The data given in Fig. 8 were used to calculate $\tilde{\omega}$ for increments of $y = 0.5$. The results are plotted in Fig. 21 for $x \geq 10$ and each value of β. For $\beta = 0.120$, the dimensionless profiles do not define a single curve. However, for $\beta = 0.088$, the profiles at $x = 20$ and 30 are nearly identical and only slightly different from the profile at $x = 10$. Moreover, the profile at $x = 30$ for $\beta = 0.120$ is nearly identical to the $\beta = 0.088$ profiles. In addition, it is noted that the profiles for $\beta = 0.088$ do not show a systematic deviation from the curve drawn in the figure, suggesting that the deviation is at least partly due to experimental error. While the number of profiles is not sufficient to permit binding conclusions, it appears that the profiles approach a nearly self-similar form at an x within the present region of measurements. If this is accepted, then an extrapolation of the curves for $(y_e)_{H_2}$ and $(\omega_{H_2})_w$, given in Figs. 16 and 20, respectively, can be used to estimate concentration profiles for $x > 30$.

CONCLUSIONS AND RECOMMENDATIONS

Conclusions

Detailed probe measurements have been used to deduce the flow field development for parallel injection of hydrogen at Mach 1.19 from a rectangular wall-slot into a Mach 2.1 airstream. Two conditions of initial hydrogen-to-air mass flux ratio were tested. On the basis of the data analysis, the following conclusions are stated:

1) The good agreement obtained between measured total hydrogen flow rates and area-integrated mass flux distributions gives confidence in the experimental results.

2) The turbulent mixing layer thicknesses grow at a nearly linear rate beyond a downstream distance which, for the present test conditions, is approximately 10 slot heights.

3) Mixing layer growth rates for species and energy are apparently equal, and they exceed the momentum layer growth rate.

4) The layer growth rates for all quantities increase as the initial hydrogen-to-air mass flux ratio is decreased, even though the initial momentum flux ratio is maintained constant. The data indicate that the effect is largest for momentum transfer.

5) For downstream distances of the order of 10 or more slot heights, the decay rates of species mass fraction and velocity maxima increase with decreasing mass flux ratio.

6) The species mass fraction profiles appear to approach a self-similar condition at a downstream distance that decreases with decreasing mass flux ratio and which does not exceed 30 slot heights for the present test conditions.

7) The results of this study confirm the conclusion that, in a variable density, variable pressure flow field, the transfer layer boundaries must be related to the proper flux vectors, rather than to flow field properties such as velocity or temperature.

Recommendations

Recommendations for future work to extend and complement the present effort are listed below:

1) To provide additional data necessary for an analytical solution of this problem, future work should include more detailed measurements of the wall-adjacent flow field with a view toward assessing the relevancy of a two-layer flow model.

2) Future tests should include a wider variation of initial conditions. In addition to varying injectant-to-freestream mass flux ratio, the effect of varying momentum flux ratio should be evaluated. Measurements should be taken at larger downstream distances in order to fully assess the attainment of self-similarity in the flow property profiles.

3) Eventually, tests should be conducted in which the effect of chemical reaction on the mixing process is evaluated.

APPENDIX

Method of Flow Field Calculations

The method used to deduce flow field properties from the experimental data is described herein. The data treatment is based on the following assumptions:

(1) The experimental probes respond only to the axial motion of the flow, or, equivalently, the motion is one-dimensional.

(2) The specific heat ratio is constant at $\gamma = 1.4$ for H_2-air mixtures of arbitrary composition.

(3) The mean flow is steady.

The surface pressure coefficient, C_p, of the cone-static-pressure probe is defined as:

$$C_p \equiv (p_c - p)/(\gamma p M^2/2) \tag{A-1}$$

where p is freestream static pressure, p_c is the average of the four cone-surface-pressure measurements and M is Mach number. The measured pitot-pressure, p_t', is introduced into Eq. (A-1), and the equation is rewritten as:

$$p_c/p_t' = (p/p_t') \; [1 + (\gamma M^2 \; C_p/2)] \tag{A-2}$$

Using the values of p/p_t' and C_p that are given as a function of M in Ref. 12, Eq. (A-2) is plotted versus M. The measured p_c and p_t' are then used to determine M from this plot, after which p is determined from Eq. (A-1), which can also be plotted in the form:

$$p/p_c = [1 + (\gamma M^2 \; C_p/2)]^{-1} \tag{A-3}$$

The measured H_2 mole fraction, X_{H_2}, is used to calculate the mixture molecular weight, $\mathfrak{M}$, as follows:

$$\mathfrak{M} = 2.016 \; X_{H_2} + 28.965 \; (1 - X_{H_2}) \tag{A-4}$$

where the molecular weights of H_2 and air are taken as 2.016 and 28.965, respectively. The gas constant, $\mathfrak{R}$, is then given by:

$$\mathfrak{R} = 1545/\mathfrak{M} \tag{A-5}$$

and the H_2 mass fraction, ω_{H_2}, is given by:

$$\omega_{H_2} = 2.016 \; X_{H_2}/\mathfrak{M} \tag{A-6}$$

If conductive and radiative heat losses are neglected, the following relation holds between measured (T_t') and actual (T_t) stagnation temperatures:

$$r = (T_t' - T)/(T_t - T) \qquad \text{(A-7)}$$

where T is static temperature and r is the probe recovery factor (Ref. 13). In general, r is a function of Reynolds and Prandtl numbers. However, in this report r is assumed constant at 0.948, which is the value required to give agreement between the measured and known air (free-stream) stagnation temperatures. The energy equation for adiabatic flow in the form:

$$T_t/T = 1 + (\gamma - 1)\, M^2/2 \qquad \text{(A-8)}$$

is combined with Eq. (A-7) to give

$$T/T_t' = [1 + r\, (\gamma - 1)\, M^2/2]^{-1} \qquad \text{(A-9)}$$

from which T is determined. The mixture enthalpy (per unit mass), h, is given by

$$h = \omega_{H_2}\, h_{H_2} + (1 - \omega_{H_2})\, h_{air} \qquad \text{(A-10)}$$

The H_2 and air enthalpies are determined versus T from Ref. 14.

The remaining properties are calculated from:

Speed of sound definition: $u = M\, (\gamma g \Re T)^{\frac{1}{2}}$ (A-11)

Equation of state: $\rho = p/\Re T$ (A-12)

Mass fraction definition: $\rho_{H_2} = \omega_{H_2}\, \rho$ (A-13)

REFERENCES

1. Weinstein, Alvin S.: Diffusion of Momentum from Free and Confined Slot Jets into Moving Secondary Stream. Ph.D. Thesis, Carnegie Institute of Technology, May 1955.

2. Schwarz, W. H.; and Cosart, W. P.: The Two-Dimensional Turbulent Wall-Jet. J. Fluid Mechanics, vol. 10, part 4, June 1961, pp. 481-495.

3. Kruka, V.; and Eskinazi, S.: The Wall-Jet in a Moving Stream. J. Fluid Mechanics, vol. 20, part 4, Dec. 1964, pp. 555-579.

4. Seban, R. A.; and Back, L. H.: Velocity and Temperature Profiles in Turbulent Boundary Layers with Tangential Injection. J. Heat Transfer, Trans. ASME, series C, vol. 84, Feb. 1962, pp. 45-54.

5. Goldstein, R. J.; Eckert, E. R. G.; Tsou, F. K.; and Haji-Sheikh, A.: Film Cooling with Air and Helium Injection through a Rearward-Facing Slot into a Supersonic Air Flow. AIAA Journal, vol. 4, no. 6, June 1966, pp. 981-985.

6. Peake, D. J.: The Use of Air Injection to Prevent Separation of the Turbulent Boundary Layer in Supersonic Flow. C. P. No. 890, Ministry of Aviation, Aeronautical Research Council, London, 1966. (Also available as NASA N67-21194.)

7. Dunn, J.; Agnone, A.; Feeley, H.; and Soll, D.: An Experimental Investigation of Supersonic Turbulent Slot Injection. TR-420, General Applied Science Laboratories, Westbury, New York, June 1964.

8. Gilreath, Harold E.; and Schetz, Joseph A.: A Study of Tangential Slot Injection in Supersonic Flow. Aero. Report No. 66-2, University of Maryland, College Park, Maryland, August 1966.

9. Shapiro, Ascher H.: The Dynamics and Thermodynamics of Compressible Flow, Vol. I. Ronald Press, New York, 1953, pp. 507-516.

10. Orth, R. C.; Schetz, J. A.; and Billig, F. S.: The Interaction and Penetration of Gaseous Jets in Supersonic Flow. NASA CR-1386, 1969.

11. Dorrance, William H.: Viscous Hypersonic Flow. McGraw-Hill, New York, 1962, p. 182.

12. Ames Research Staff: Equations, Tables and Charts for Compressible Flow. NACA Report 1135, 1953.

13. Volluz, R. J.: Handbook of Supersonic Aerodynamics, Section 20, Wind Tunnel Instrumentation and Operation. NAVORD Report 1488, vol. 6, Jan. 1961, pp. 279-286.

14. Hilsenrath, Joseph, et al.: Tables of Thermal Properties of Gases. Circular 564, National Bureau of Standards, U. S. Department of Commerce, Nov. 1955.

TABLE I

TEST CONDITIONS AND FIGURE LEGEND

RUN	T_{t_e} (°R)	p_{t_e} (psia)	T_{t_j} (°R)	p_{t_j} (psia)	x	LEGEND	FIGURE
50	522	137	550	35.2	2	●	6a, 7a
53	527	133	561	36.3	↓	■	↓
57	531	135	557	35.7	↓	▲	↓
51	524	136	552	35.3	4	○	↓
54	525	135	564	36.4	↓	□	↓
58	529	135	559	36.7	↓	△	↓
52	524	135	554	36.4	7	●✓	↓
55	530	135	558	35.9	↓	■✓	↓
59	528	135	560	35.3	↓	▲✓	↓
33	524	134	543	36.2	10	●	6b
36	528	134	547	35.9	↓	■	6b, 7b
29	526	135	546	35.4	↓	▲	↓
34	524	135	551	36.4	20	○	6b
37	526	134	549	36.2	↓	□	6b, 7b
31	517	135	536	35.8	↓	△	↓
35	524	134	549	37.0	30	●✓	6b
38	526	135	547	35.8	↓	■✓	6b, 7b
32	515	133	534	36.8	↓	▲✓	↓
73	477	134	960	35.5	10	●	6c, 7c
76	491	136	↓	35.7	↓	■	↓
79	489	135	↓	33.7	↓	▲	↓
74	478	136	↓	35.3	20	○	↓
77	489	135	↓	35.3	↓	□	↓
80	482	135	↓	34.4	↓	△	↓
75	486	133	↓	35.5	30	●✓	↓
78	487	137	↓	35.3	↓	■✓	↓
81	482	134	↓	34.4	↓	▲✓	↓
60	524	133	554	35.8	2	●	8a
63	532	136	564	35.4	↓	■	↓
66	513	133	549	34.4	↓	▲	↓
61	534	132	550	35.9	4	○	↓
64	549	134	585	36.3	↓	□	↓
67	508	133	556	35.0	↓	△	↓
62	533	133	556	36.0	7	●✓	↓
65	537	135	568	35.0	↓	■✓	↓
68	517	133	553	35.0	↓	▲✓	↓
33	524	134	543	36.2	10	●	8b
5	511	134	540	36.8	↓	■	↓
9	518	135	533	35.9	↓	▲	↓
20	521	135	544	35.2	↓	◆	↓
34	524	135	551	36.4	20	○	↓
7	514	135	534	35.4	↓	□	↓
11	509	135	527	36.4	↓	△	↓
24	518	135	548	36.7	↓	◇	↓
30	519	136	535	35.3	30	●✓	↓
8	512	135	537	36.4	↓	■✓	↓
22	510	135	535	35.4	↓	▲✓	↓
100	487	134	960	34.0	10	●	8c
95	505	134	↓	35.3	↓	■	↓
92	498	134	↓	35.3	↓	▲	↓
83	484	135	↓	34.0	↓	◆	↓
99	486	133	↓	35.0	20	○	↓
90	479	136	↓	35.0	↓	□	↓
93	494	135	↓	34.7	↓	△	↓
84	478	135	↓	34.4	↓	◇	↓
98	485	135	↓	35.7	30	●✓	↓
91	478	133	↓	34.5	↓	■✓	↓
94	494	135	↓	35.3	↓	▲✓	↓
97	481	133	↓	35.0	↓	◆✓	↓
86	496	136	↓	34.5	10	●	9
95	505	134	↓	35.3	↓	■	↓
92	498	134	↓	35.3	↓	▲	↓
99	486	133	↓	35.0	20	○	↓
96	483	134	↓	35.0	↓	□	↓
93	494	135	↓	34.7	↓	△	↓
98	485	135	↓	35.7	30	●✓	↓
97	481	133	↓	35.0	↓	■✓	↓
94	494	135	↓	35.3	↓	▲✓	↓

TABLE II
INITIAL FLOW FIELD PROPERTIES

SERIES	x	T_{t_e} (°R)	T_{t_j} (°R)	T_t (°R)	p_{t_e} (psia)	p_{t_j} (psia)	M_e	M_j	T_e (°R)	T_j (°R)	p_e (psia)	p_j (psia)
1	2,4,7	527	558	543	135	35.5	2.10	1.19	280	435	14.8	14.8
2	10,20,30	520	541	530	↓	↓	↓	↓	276	422	↓	↓
3	10,20,30	487	960		↓	↓	↓	↓	259	748	↓	↓

SERIES	x	ρ_e (10^{-1} LB/FT^3)	ρ_j (10^{-3} LB/FT^3)	u_e (FT/SEC)	u_j (FT/SEC)	ρ_j/ρ_e (10^{-2})	u_j/u_e	T_j/T_e	β	R_e (1) (10^5)	R_j (1) (10^5)
1	2,4,7	1.43	6.39	1723	4611	4.48	2.68	1.55	0.120	6.27	1.03
2	10,20,30	1.45	6.59	1710	4542	4.55	2.66	1.53	0.121	6.40	1.07
3	10,20,30	1.54	3.72	1656	6048	2.41	3.65	2.89	0.088	7.00	0.55

(1) BASED ON SLOT HEIGHT, 7/32 INCH.

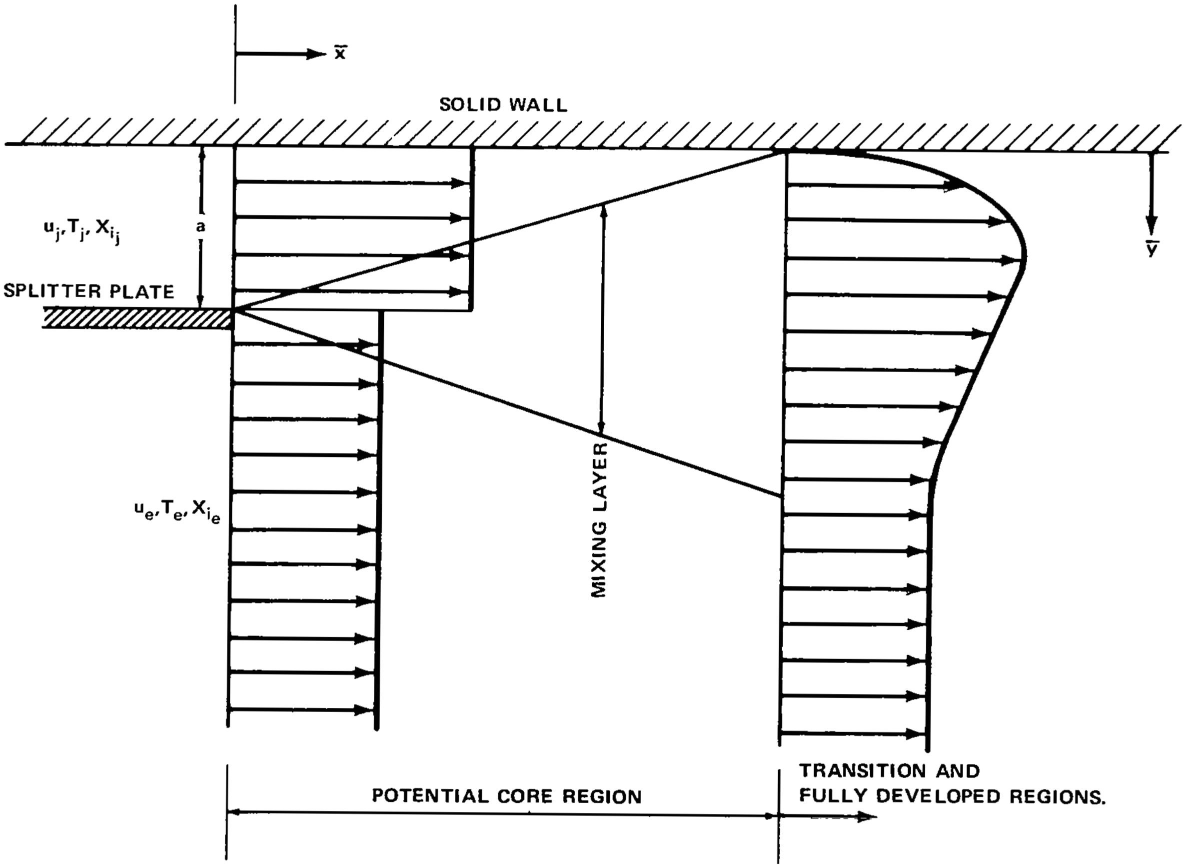

FIG. 1 SCHEMATIC OF WALL-SLOT INJECTION FLOW

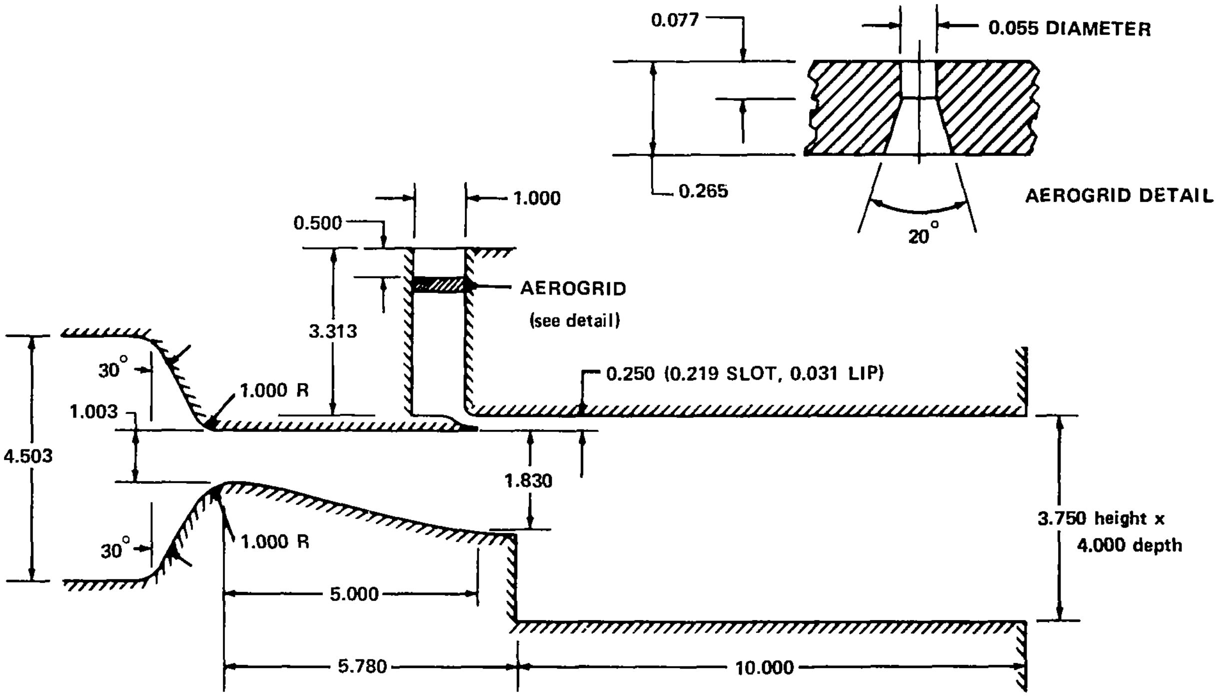

DIMENSIONS ARE IN INCHES

FIG. 2 SCHEMATIC OF EXPERIMENTAL MODEL

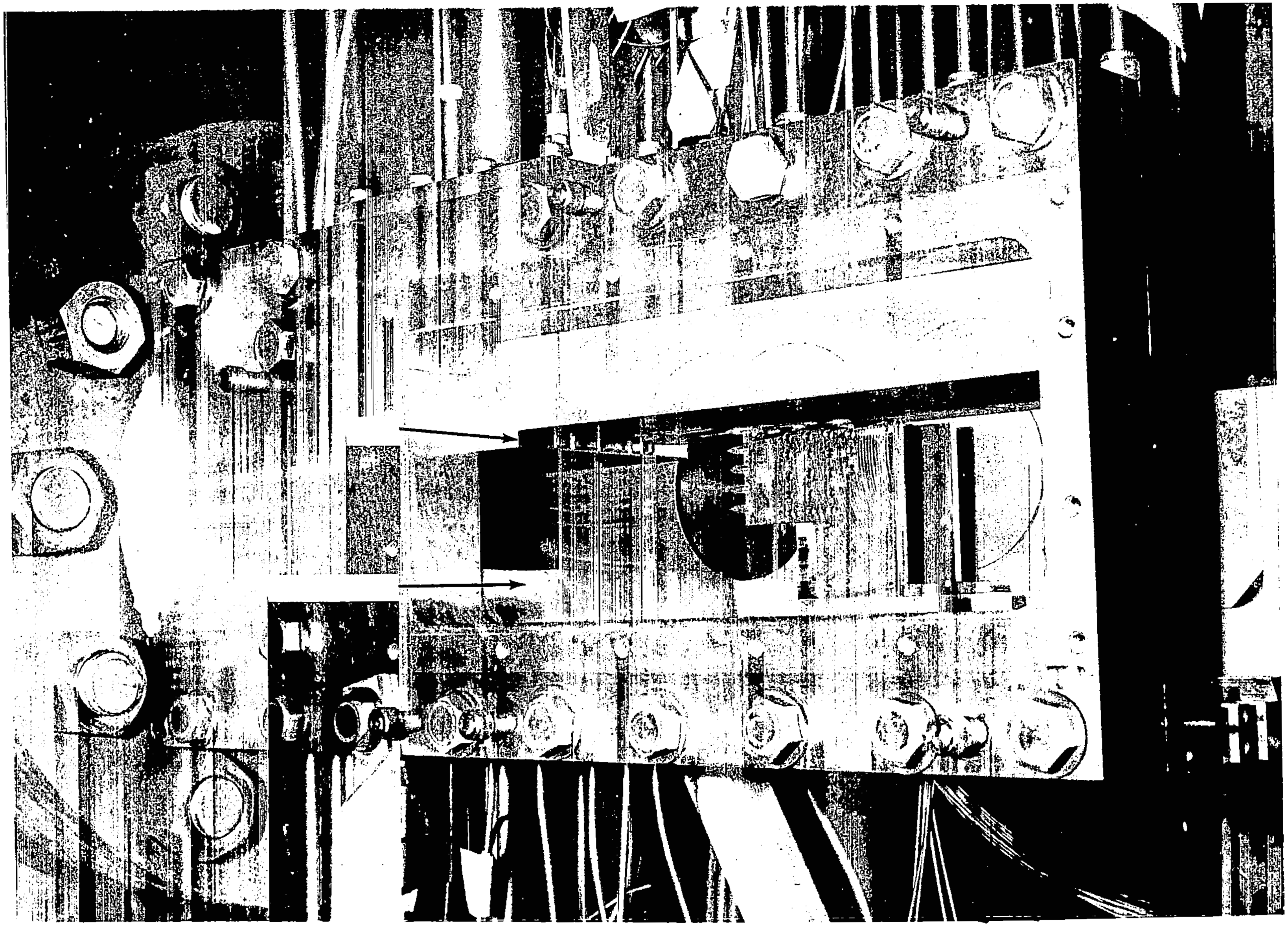

Fig. 3 EXPERIMENTAL MODEL (NEAR WINDOW FRAME REMOVED).

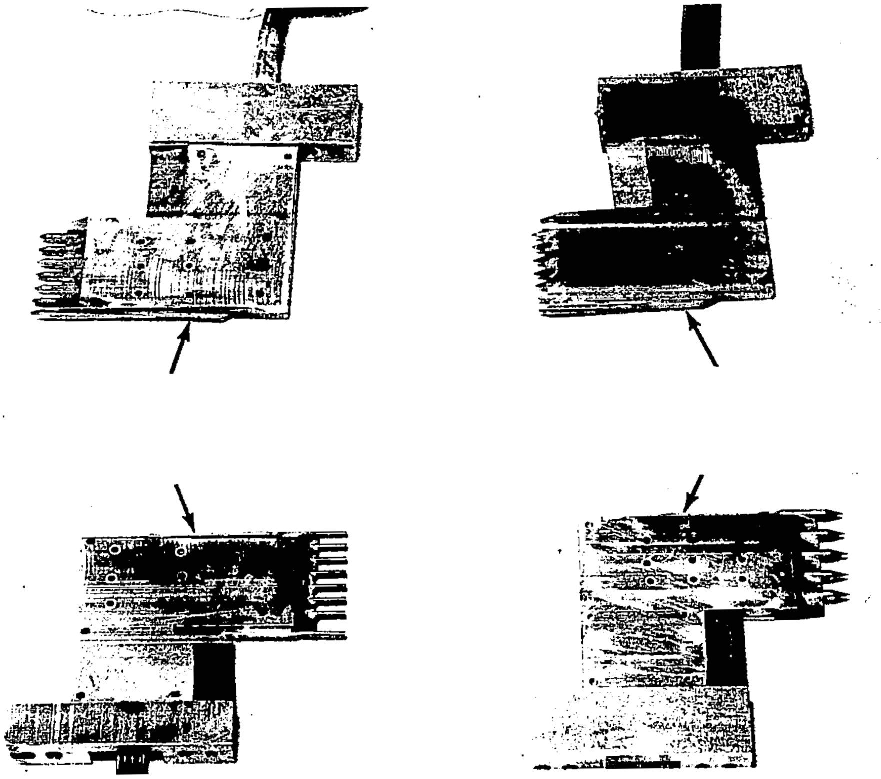

Fig. 4 IN-STREAM INSTRUMENTATION

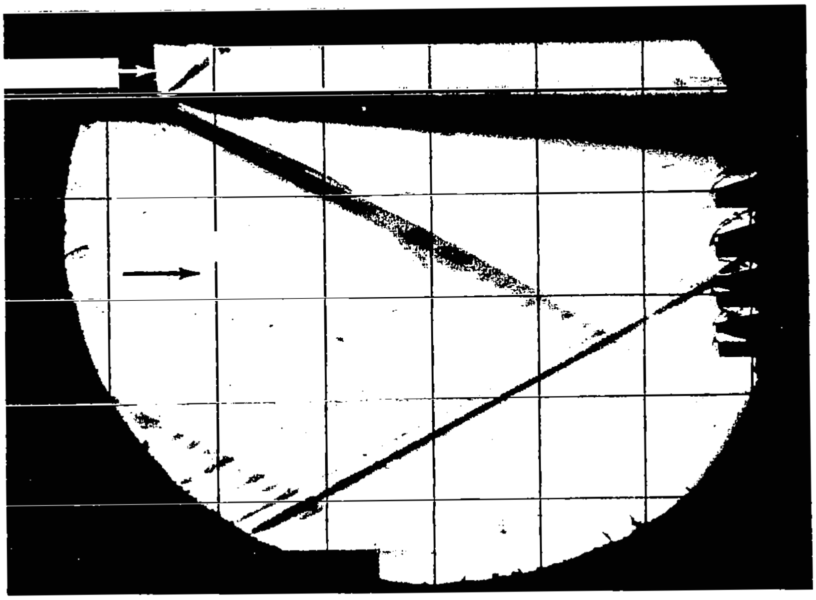

Fig. 5 SCHLIEREN PHOTOGRAPH OF MIXING FLOW FIELD

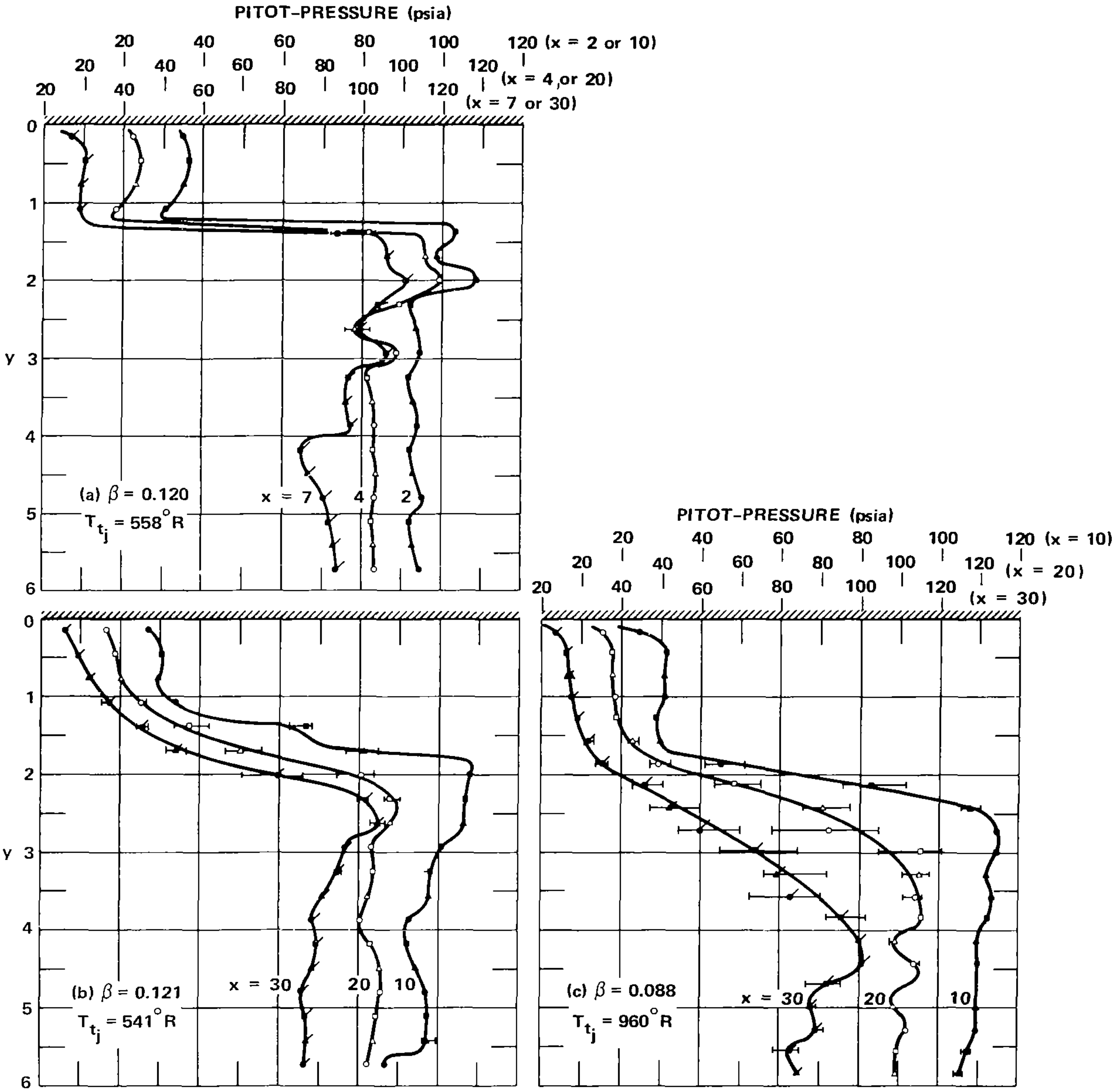

FIG. 6 PITOT-PRESSURE DATA

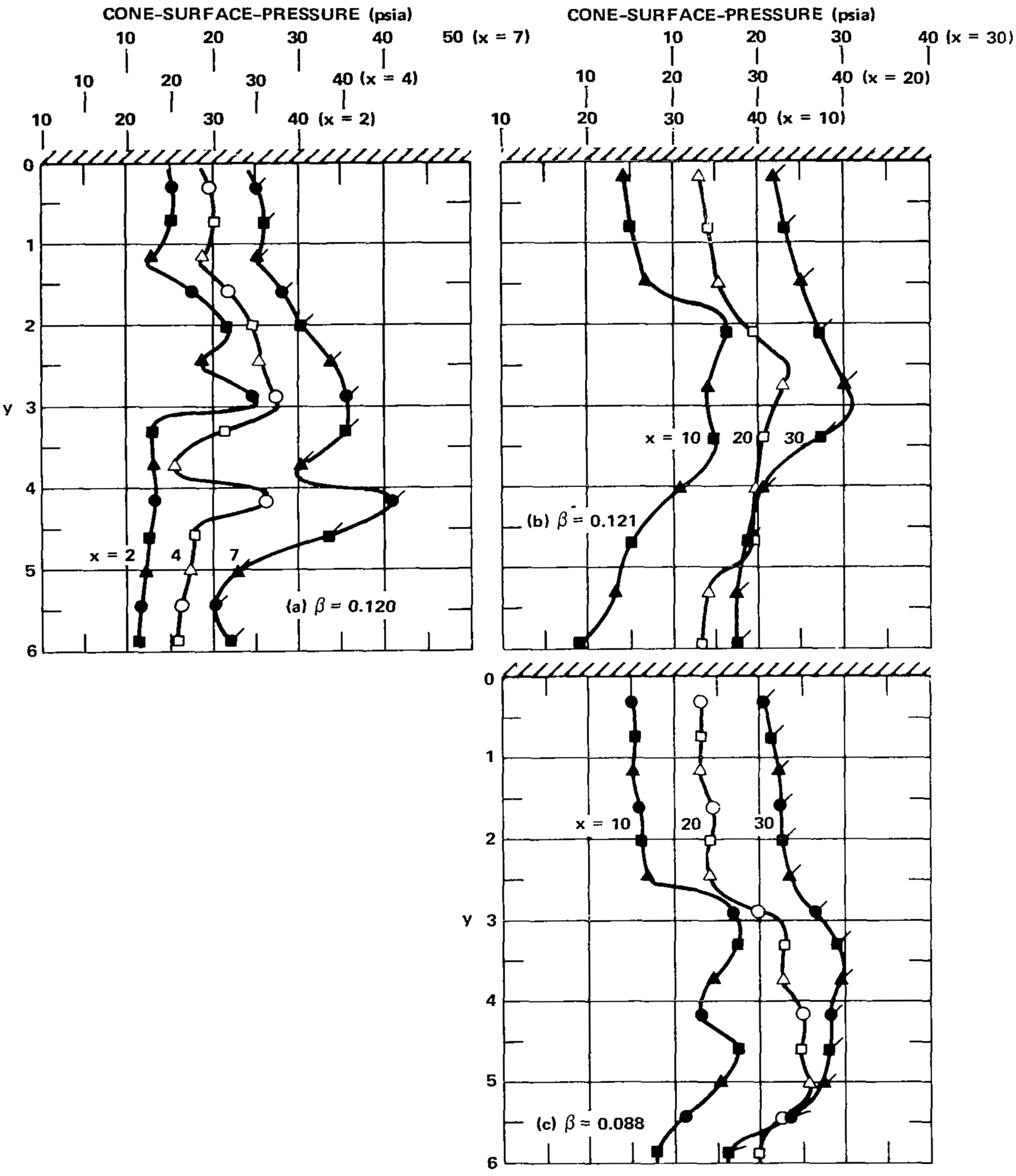

FIG. 7 CONE-STATIC-PRESSURE DATA

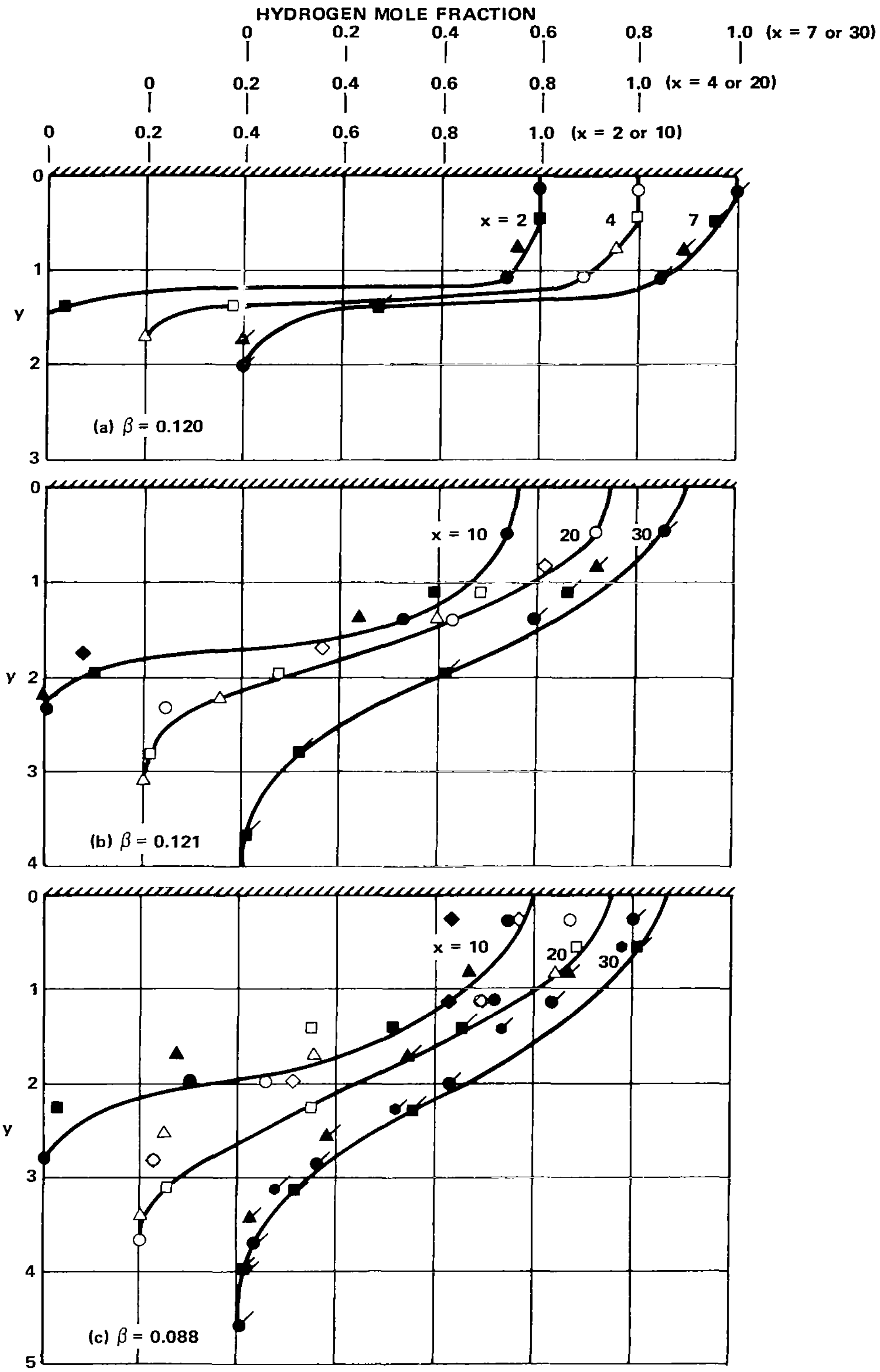

FIG. 8 GAS SAMPLE DATA

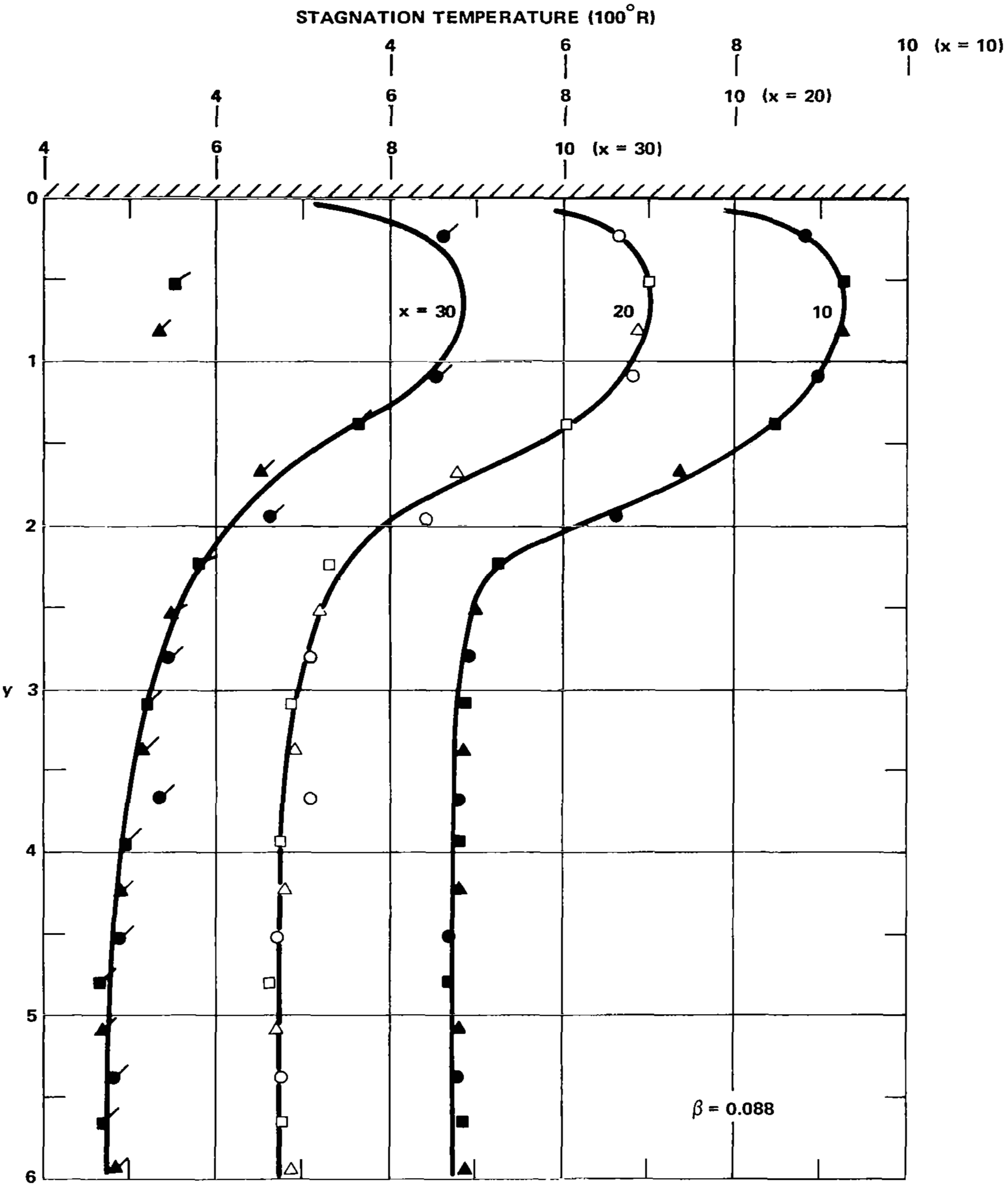

FIG. 9 STAGNATION TEMPERATURE DATA

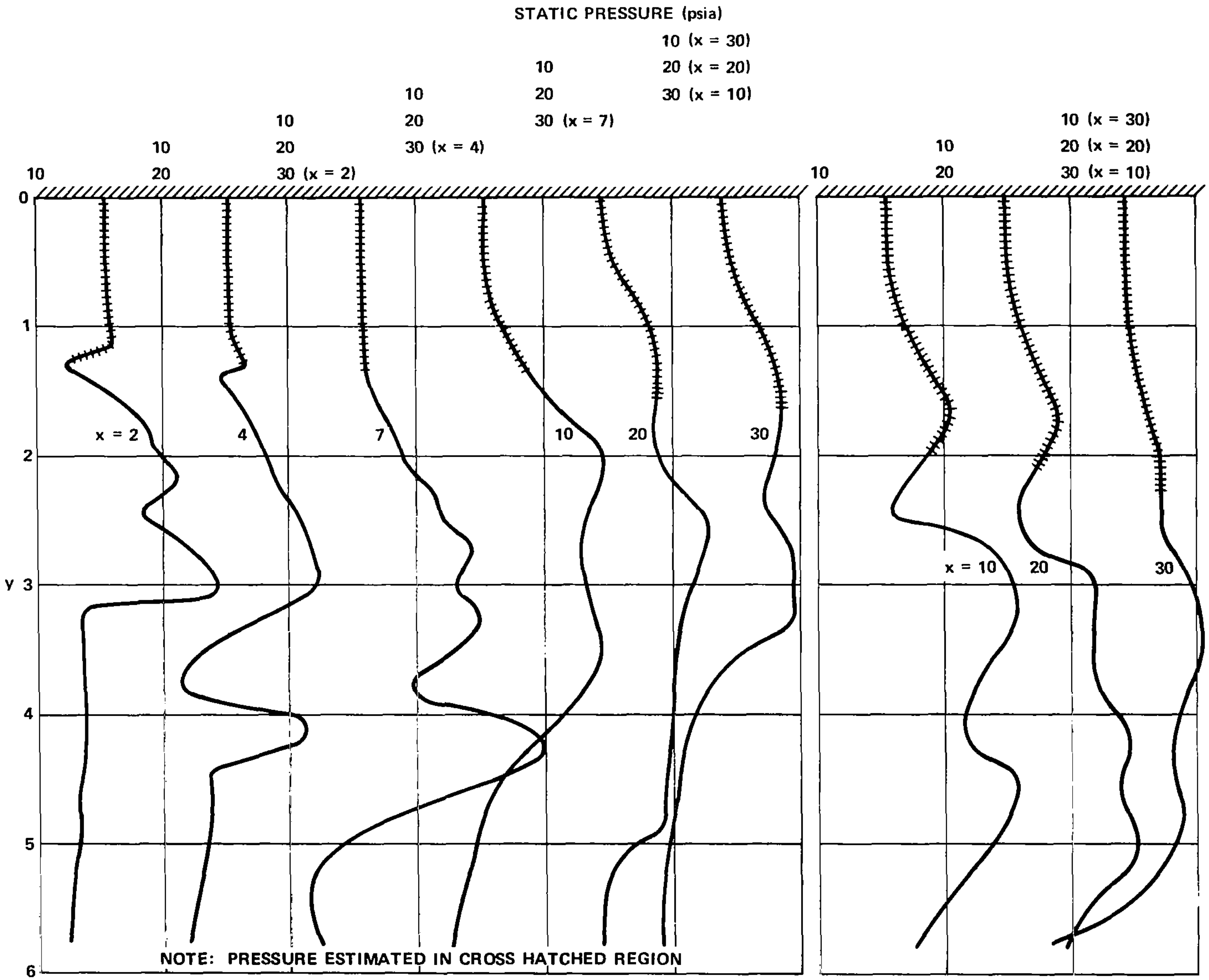

(a) Ambient T_{t_j}; $\beta = 0.120$ for x = 2 - 7; 0.121 for x = 10 - 30

(b) $T_{t_j} = 960^\circ$ R; $\beta = 0.088$

FIG. 10 DEDUCED STATIC PRESSURE PROFILES

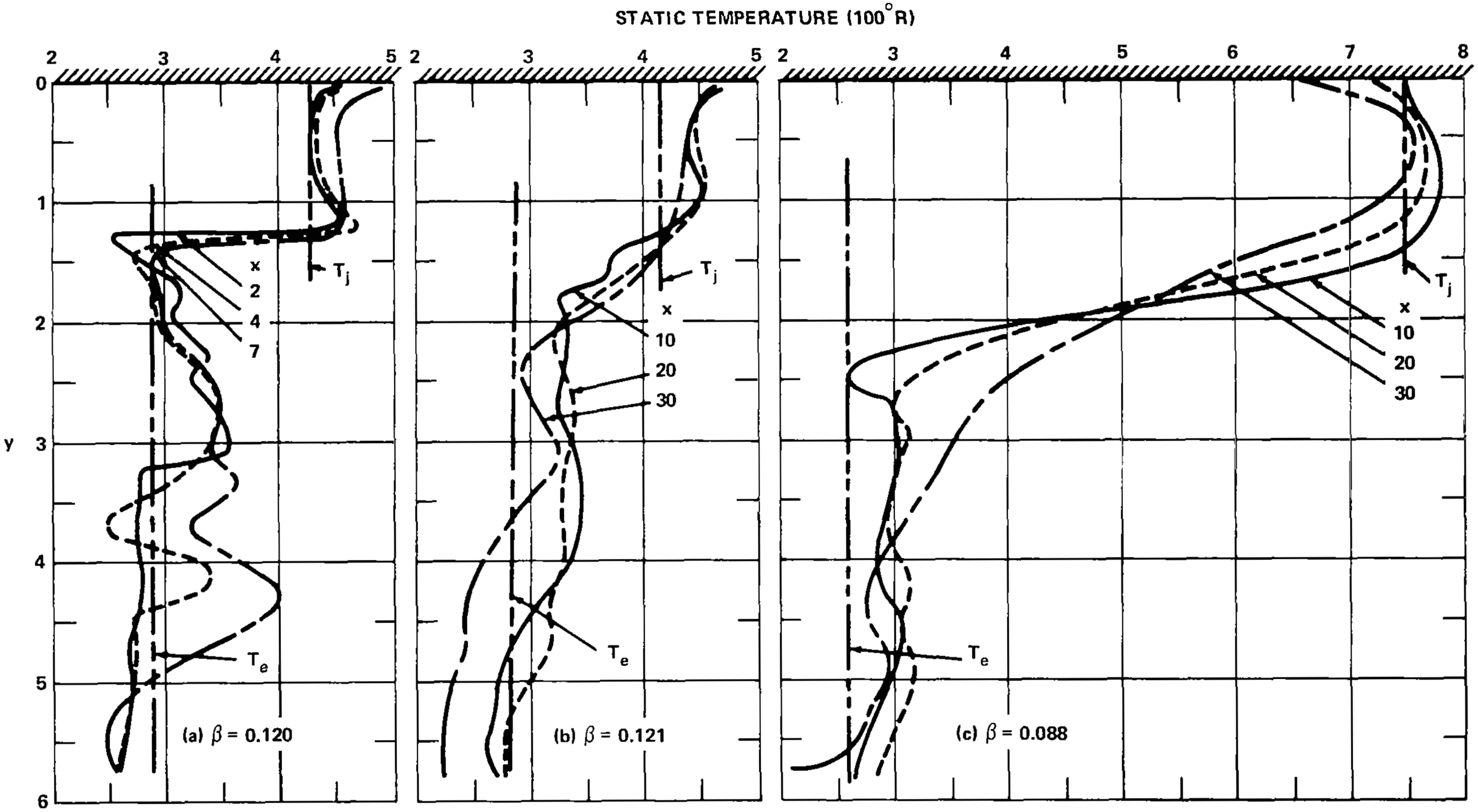

FIG. 11 DEDUCED STATIC TEMPERATURE PROFILES

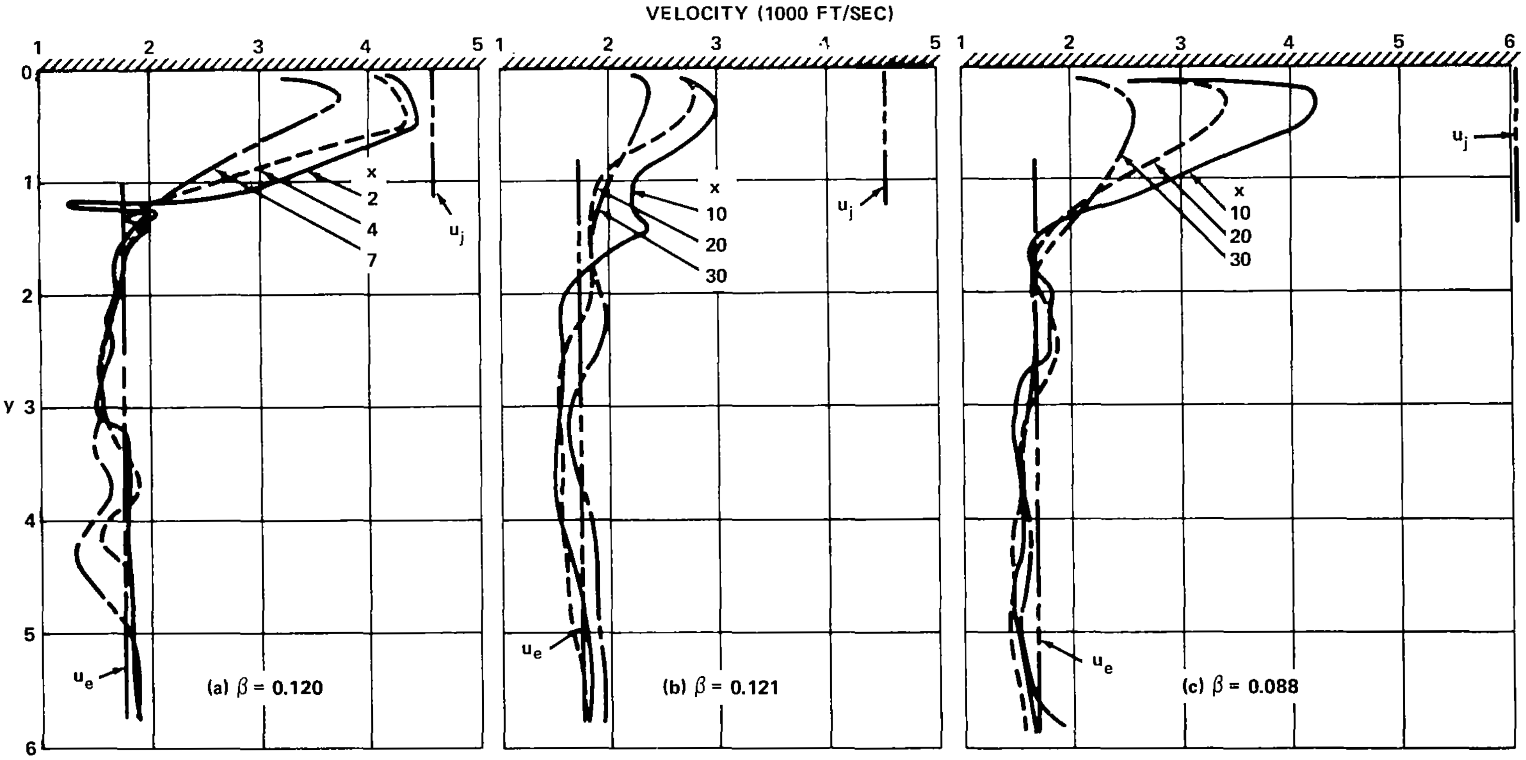

FIG. 12 DEDUCED VELOCITY PROFILES

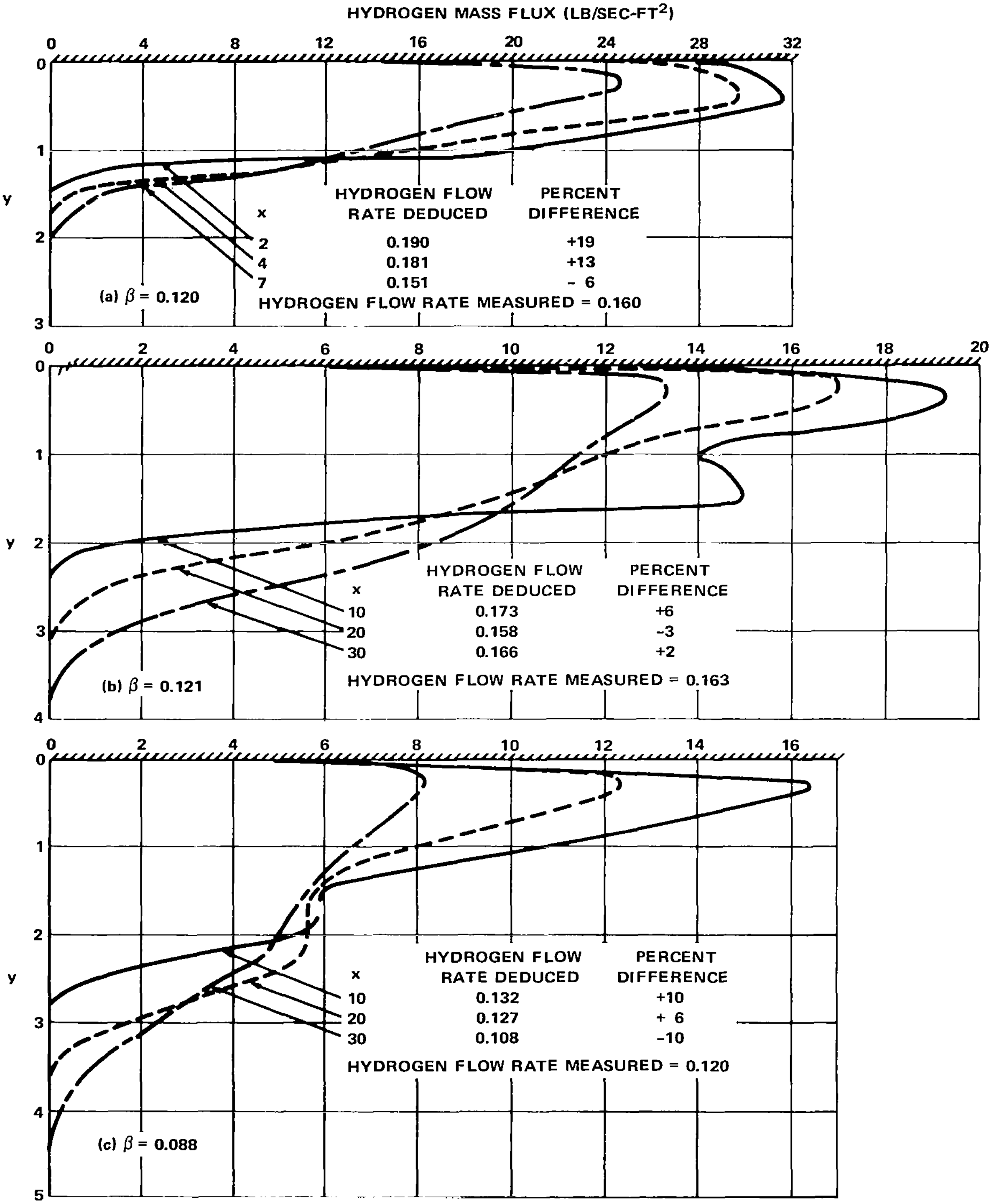

(a) β = 0.120

x	HYDROGEN FLOW RATE DEDUCED	PERCENT DIFFERENCE
2	0.190	+19
4	0.181	+13
7	0.151	- 6

HYDROGEN FLOW RATE MEASURED = 0.160

(b) β = 0.121

x	HYDROGEN FLOW RATE DEDUCED	PERCENT DIFFERENCE
10	0.173	+6
20	0.158	-3
30	0.166	+2

HYDROGEN FLOW RATE MEASURED = 0.163

(c) β = 0.088

x	HYDROGEN FLOW RATE DEDUCED	PERCENT DIFFERENCE
10	0.132	+10
20	0.127	+ 6
30	0.108	-10

HYDROGEN FLOW RATE MEASURED = 0.120

FIG. 13 DEDUCED HYDROGEN MASS FLUX DISTRIBUTIONS

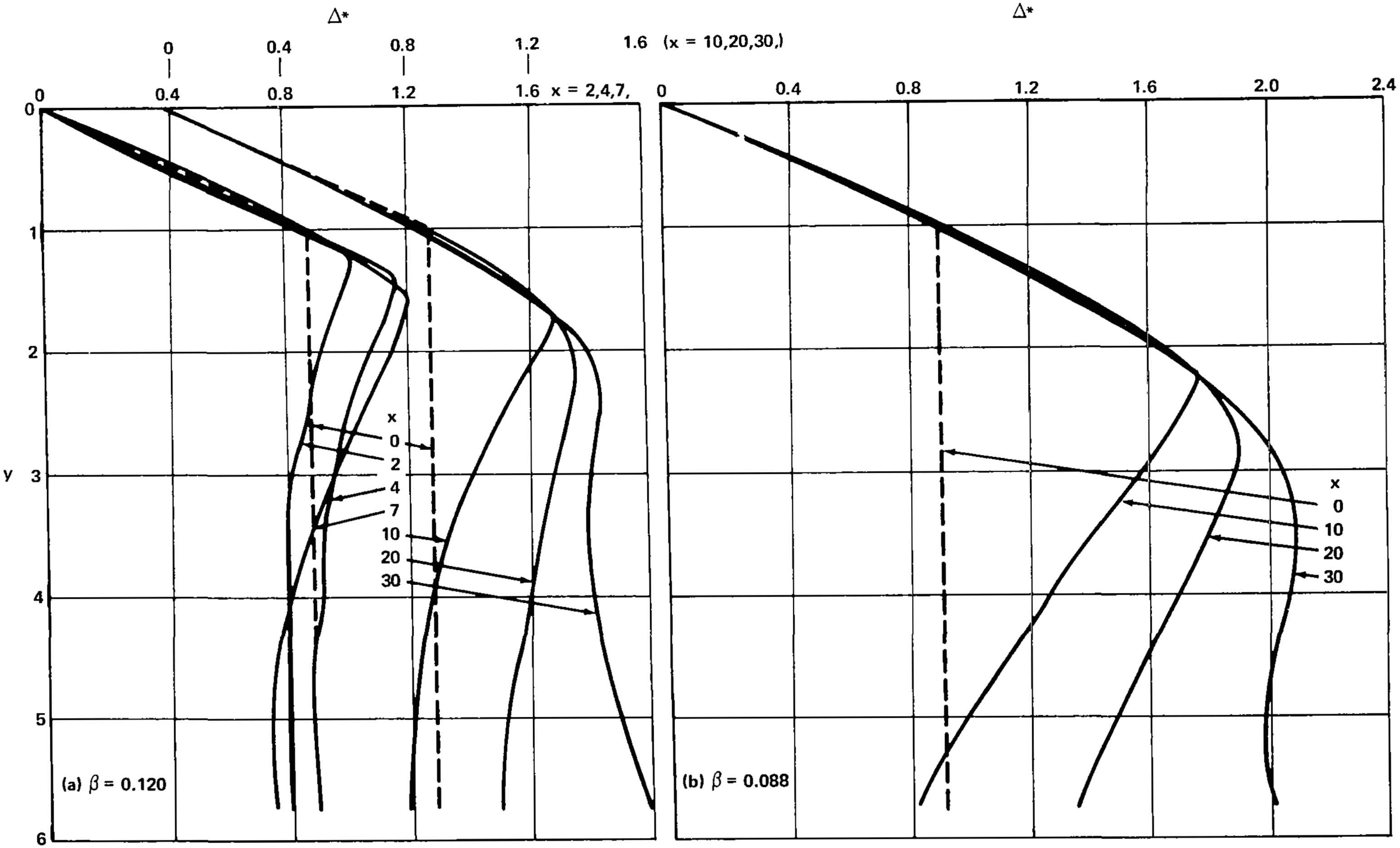

FIG. 14 NORMAL DISTRIBUTIONS OF INTEGRAL RELATED TO NORMAL VELOCITY COMPONENT.

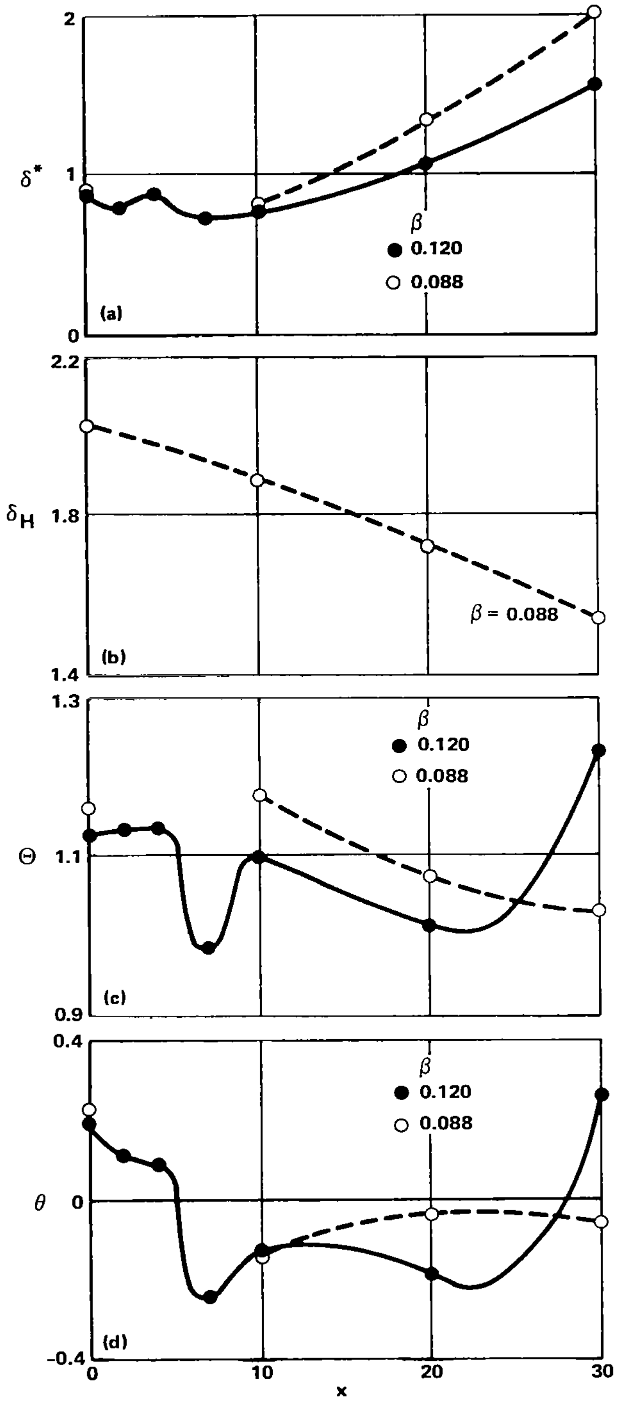

FIG. 15 AXIAL VARIATION OF INTEGRAL PROPERTIES ALONG PLANE AT y = 5.75

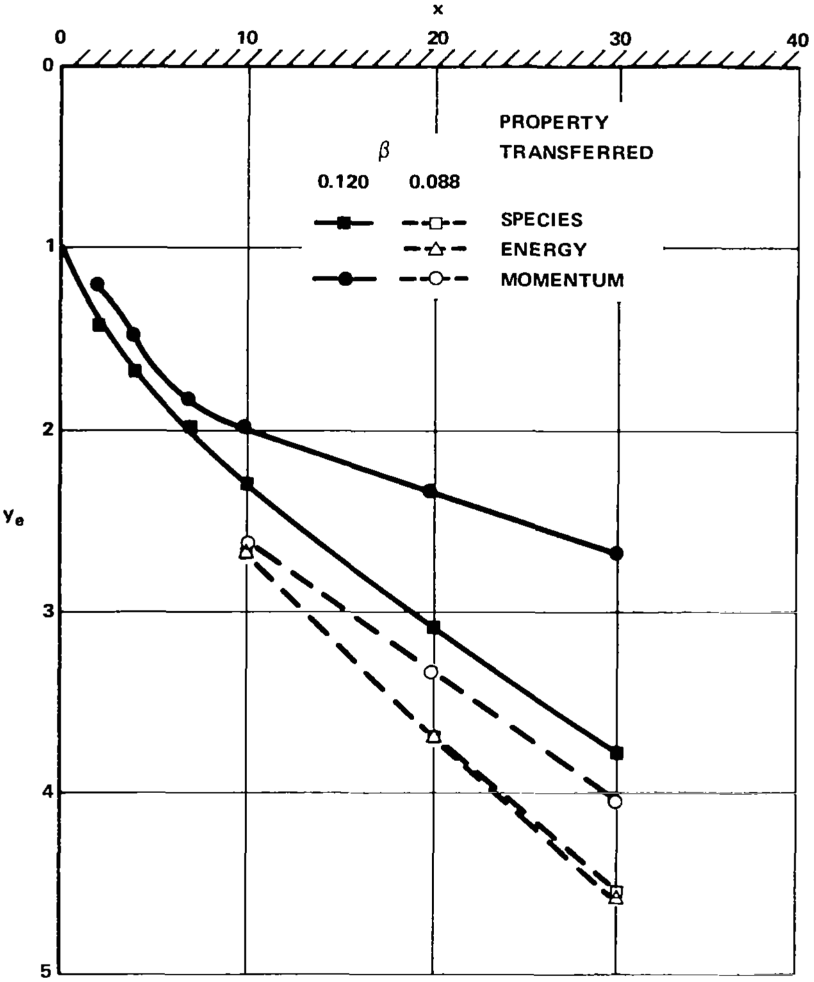

FIG. 16 COMPARISON OF THICKNESSES OF TRANSFER LAYERS.

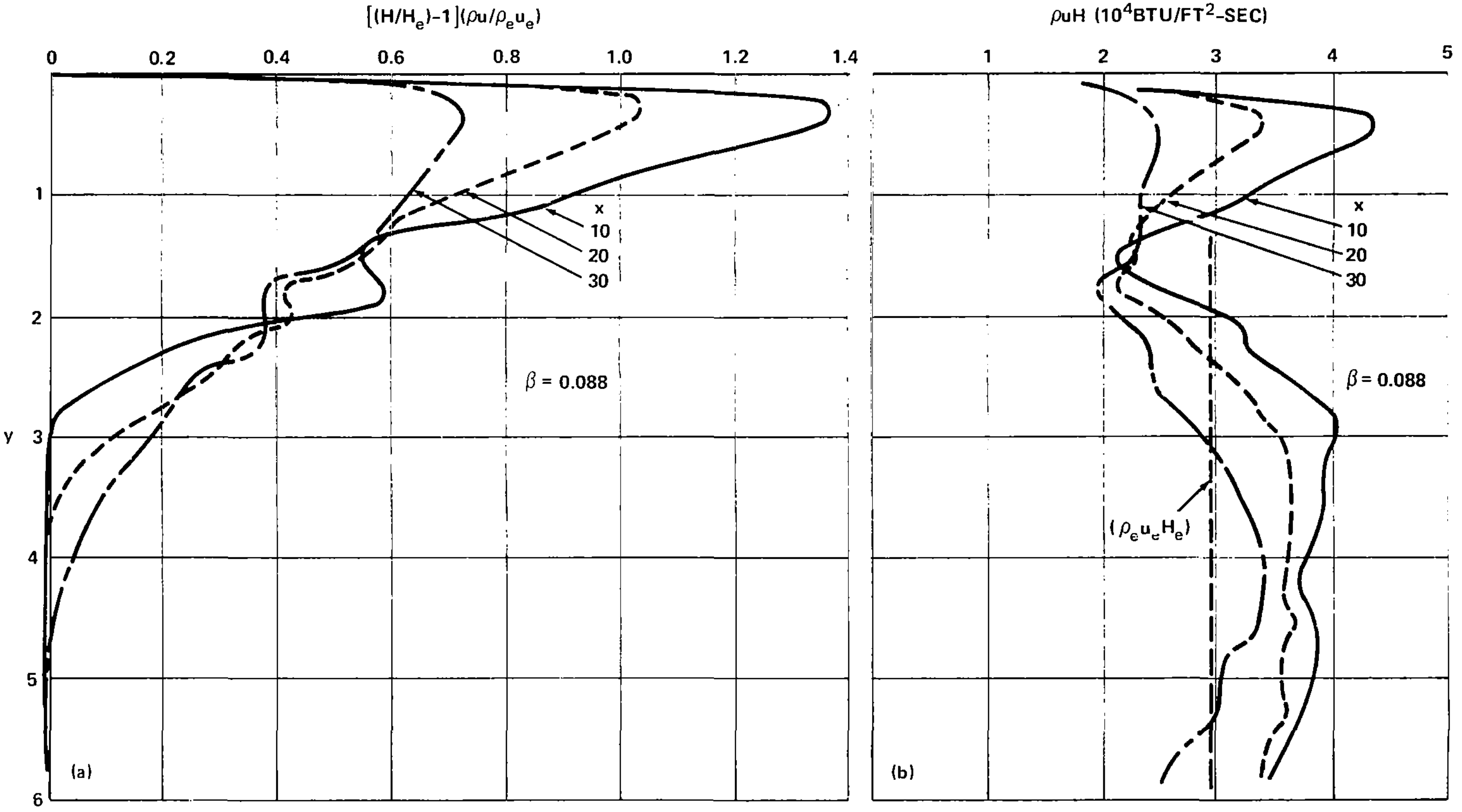

FIG. 17 NORMAL DISTRIBUTION OF QUANTITIES RELATED TO ENERGY TRANSFER

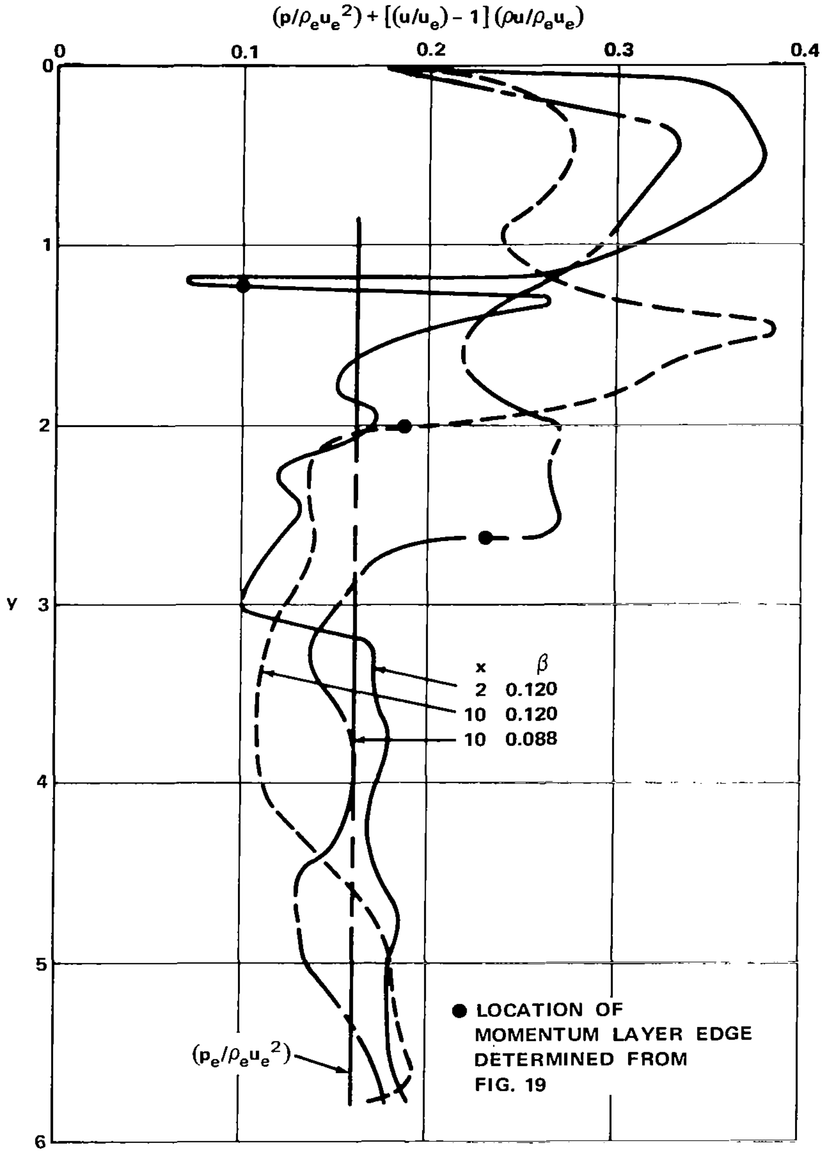

FIG. 18 NORMAL DISTRIBUTION OF QUANTITY RELATED TO MOMENTUM TRANSFER.

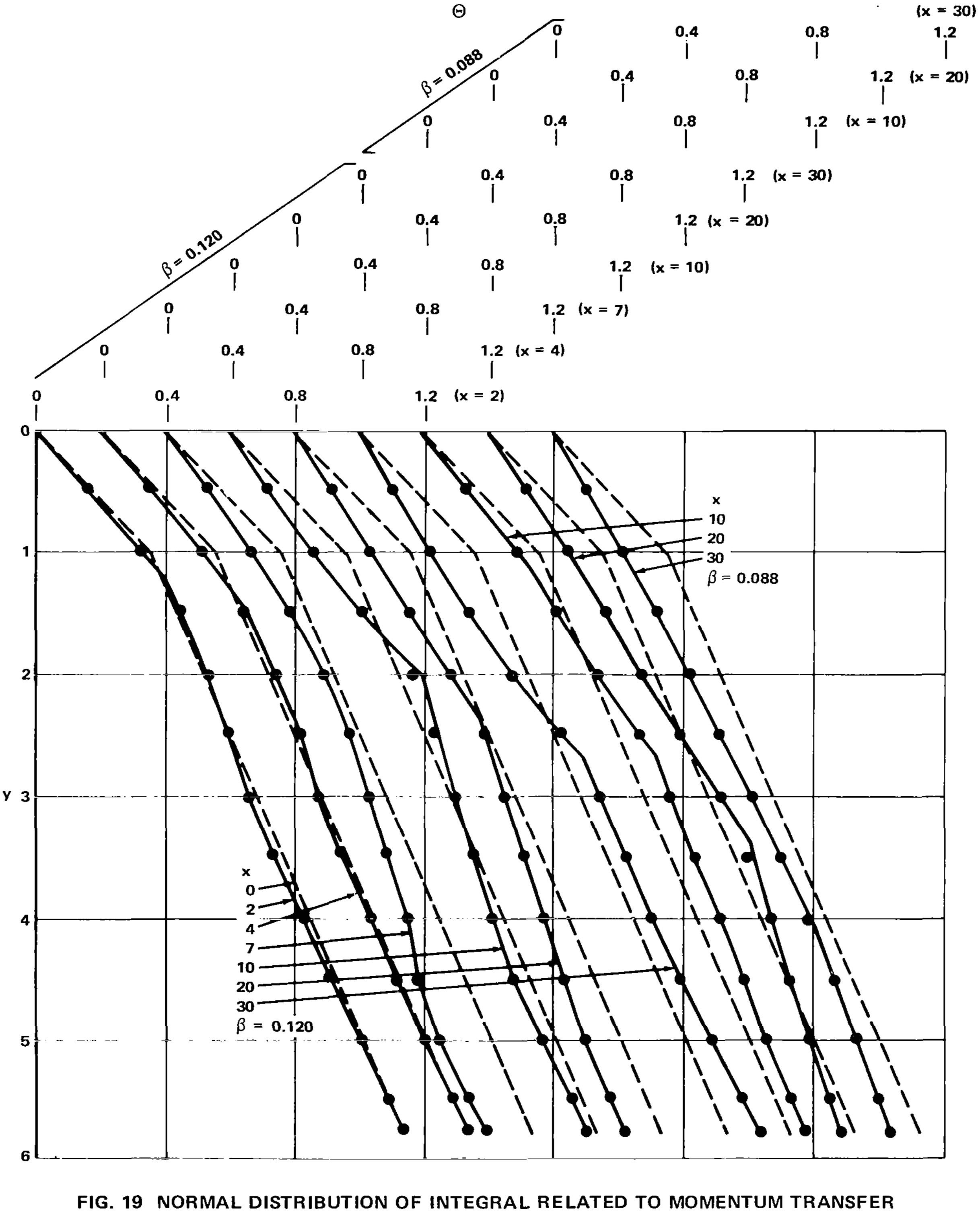

FIG. 19 NORMAL DISTRIBUTION OF INTEGRAL RELATED TO MOMENTUM TRANSFER

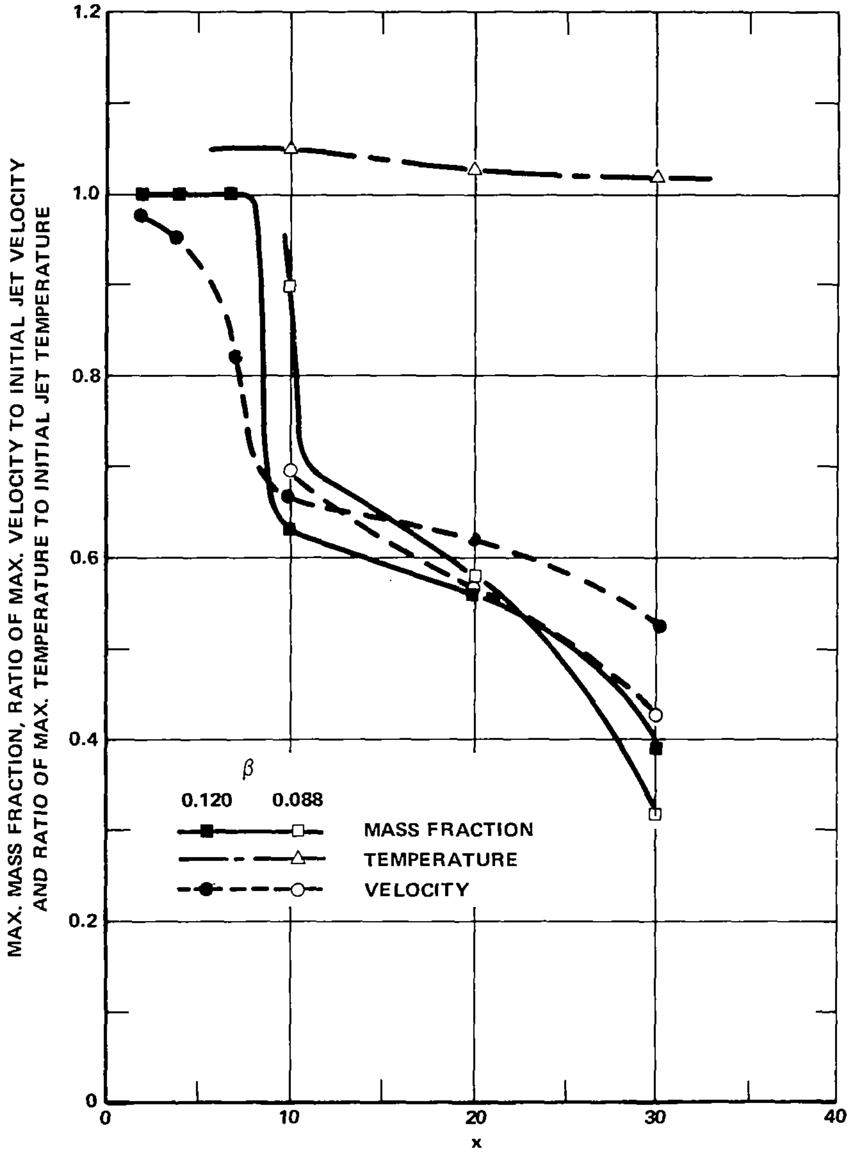

FIG. 20 COMPARISON OF DECAY RATES OF MASS FRACTION, TEMPERATURE AND VELOCITY MAXIMA.

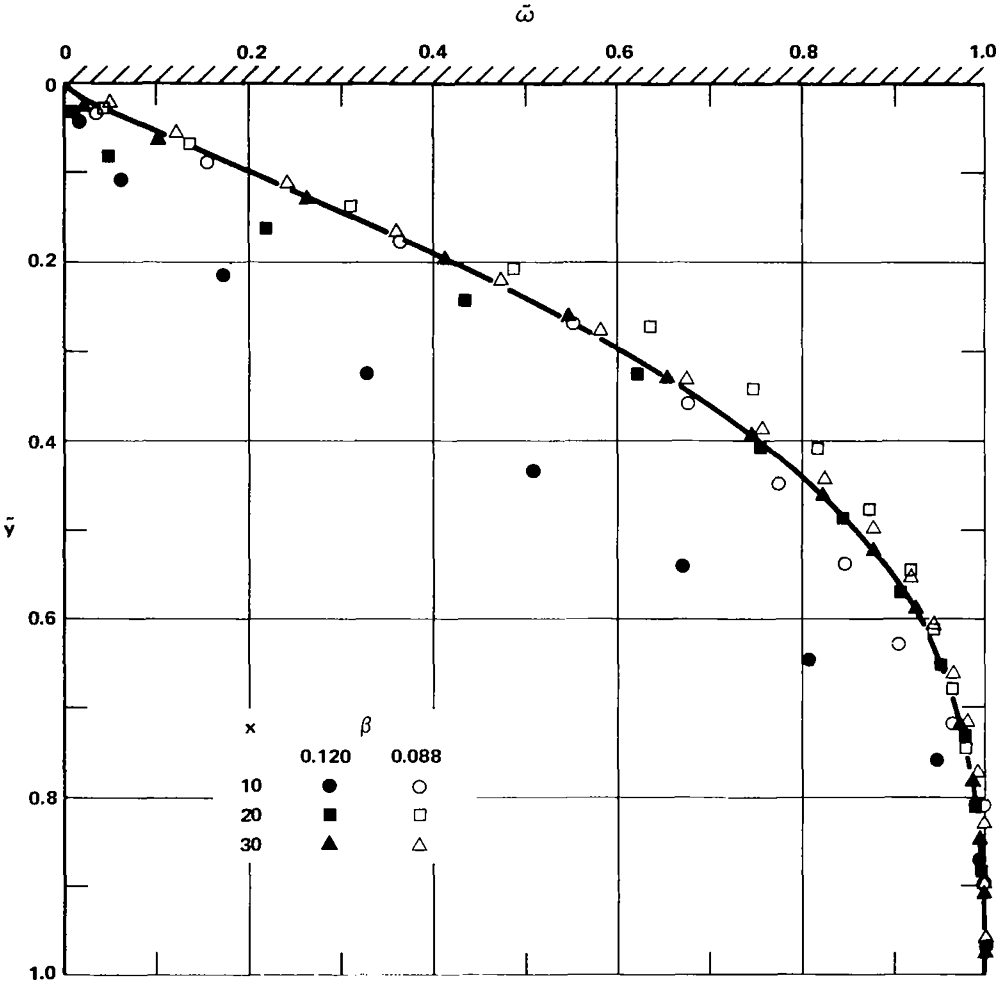

FIG. 21 A STUDY OF SIMILARITY OF MASS FRACTION DISTRIBUTIONS